On the origin of charge-density waves in select layered transition-metal dichalcogenides

2011 J. Phys.: Condens. Matter 23 213001

(http://iopscience.iop.org/0953-8984/23/21/213001)

IOP Publishing Journal of Physics: Condensed Matter
J. Phys.: Condens. Matter **23** (2011) 213001 (24pp) doi:10.1088/0953-8984/23/21/213001

TOPICAL REVIEW

On the origin of charge-density waves in select layered transition-metal dichalcogenides

K Rossnagel

Institute for Experimental and Applied Physics, University of Kiel, D-24098 Kiel, Germany

Received 9 August 2010, in final form 14 April 2011
Published 11 May 2011
Online at stacks.iop.org/JPhysCM/23/213001

Abstract
The occurrence of charge-density waves in three selected layered transition-metal dichalcogenides—1T-TaS$_2$, 2H-TaSe$_2$ and 1T-TiSe$_2$—is discussed from an experimentalist's point of view with a particular focus on the implications of recent angle-resolved photoelectron spectroscopy results. The basic models behind charge-density-wave formation in low-dimensional solids are recapitulated, the experimental and theoretical results for the three selected compounds are reviewed, and their band structures and spectral weight distributions in the commensurate charge-density-wave phases are calculated using an empirical tight-binding model. It is explored whether the origin of charge-density waves in the layered transition-metal dichalcogenides can be understood in a unified way on the basis of a few measured and calculated parameters characterizing the interacting electron–lattice system. It is found that the predictions of the standard mean-field model agree only semi-quantitatively with the experimental data and that there is not one generally dominant factor driving charge-density-wave formation in this family of layer compounds. The need for further experimental and theoretical scrutiny is emphasized.

(Some figures in this article are in colour only in the electronic version)

Contents

1. Introduction

Charge-density waves (CDWs) in low-dimensional solids are a rather old [1–8] but still vital and alluring [9–17] research topic. It is now some 35 years since CDWs in the transition-metal dichalcogenides were discovered and since this class of layered crystals consisting of three-atom-thick chalcogen–transition metal–chalcogen sandwiches initiated the popularization of the concept of a CDW [18]. Yet, although much has been learnt about the structural and electronic properties of ‘the layer compounds’ and about the nature of their various CDW phases [18–24], we are still far from understanding how and why the CDWs in these quasi-two-dimensional systems are formed. Some important aspects of the CDW phase transition in these materials are captured qualitatively by models coming under different names: Peierls instability, giant Kohn anomaly, Fermi surface nesting, band Jahn–Teller effect or excitonic insulator. But a coherent and realistic microscopic theory has not yet emerged (see, however, [23]) meaning that truly quantitative predictions of CDW properties are practically impossible. This is all the more frustrating given that the ‘standard model’ of CDW formation (one-dimensional weak-coupling mean-field theory) provides a good quantitative explanation for the occurrence of CDWs in quasi-one-dimensional solids [25] and also seems to work well for other quasi-two-dimensional systems such as the layered rare earth tritellurides [26, 27].

To make further progress at this point, we believe that the current situation regarding CDWs in transition-metal dichalcogenides, which encompasses a large body of experimental and theoretical results from the pre-cuprate era as well as recent high-resolution angle-resolved photoelectron spectroscopy (ARPES) results, must be looked at in greater detail and taken into account more seriously before one fills the gaps in understanding by suggesting novel, exotic CDW mechanisms. In this spirit, we will strictly concentrate here on the possible origin of three distinctive CDWs in three prominent members of the transition-metal dichalcogenide family, i.e. 1T-TaS$_2$, 2H-TaSe$_2$ and 1T-TiSe$_2$. Phenomena that go beyond the primary formation of the CDW, such as the dynamics of CDWs [28] or the competition between CDWs and superconductivity [29], will not be discussed. Also, the many other CDW materials with one-dimensional (1D) [25], two-dimensional (2D) [30] and three-dimensional (3D) [31, 32] band structures will not be dealt with.

For the three selected transition-metal compounds, we will specifically focus on the interpretation of the most recent, very detailed ARPES results in terms of an empirical tight-binding model and on the resulting implications for the microscopic mechanism underlying CDW formation. The working hypothesis will be that the origin of all three CDWs can be understood at least semi-quantitatively within a mean-field model, on the basis of a few measured and calculated parameters such as the transition temperature, the wavevector and amplitude of the CDW, the non-interacting electronic susceptibility, bare phonon frequencies, an electron–phonon coupling constant or the total band energy lowering in the CDW phase. The approach is that of an experimentalist and, if not providing a detailed microscopic explanation, it is at least expected to reveal the weak points in our understanding of CDW formation in the layered transition-metal dichalcogenides.

The outline of the present work is as follows. In section 2 we provide the theoretical background by summarizing the basic ideas and concepts behind CDW formation in low-dimensional systems. This is done with a narrow focus on the models that are commonly used to explain the origin of the CDWs in the layered transition-metal dichalcogenides. In section 3 we briefly review the extensive experimental and theoretical results obtained for the three selected CDW compounds, before in section 4 we seek to explain the results of recent ARPES measurements by calculating the band structures and spectral weight distributions in the CDW phases using an empirical tight-binding model. Finally, in section 5, we weave the strands together and attempt—on the basis of a few relevant parameters extracted from experiment and theory—to answer the fundamental question at the center of this work: why do CDWs occur in the layered transition-metal dichalcogenides?

2. Theoretical aspects of CDW formation

Consider a 1D metal made of a linear chain of atoms with a regular spacing a and suppose that the electron density is cosinusoidally modulated:

$$\rho(\mathbf{r}) = \rho_0(\mathbf{r})[1 + \rho_1 \cos(\mathbf{q}_0\mathbf{r} + \phi)], \tag{1}$$

where $\rho_0(\mathbf{r})$ describes the unperturbed electron density, and ρ_1, $\mathbf{q}_0$ and ϕ are the amplitude, wavevector and phase of the electron density modulation, respectively. The last term in the square bracket is called the CDW. This standing wave has a wavelength $\lambda_0 = 2\pi/|\mathbf{q}_0|$ and it causes each ion in the chain to see a different potential so that the ions move to new equilibrium positions. The resulting periodic lattice distortion (PLD) has the form

$$u_n = u_0 \sin(n|\mathbf{q}_0|a + \phi), \tag{2}$$

where the integer n defines the position of the ions and the amplitude u_0 is generally small compared to the lattice constant a. Now suppose that first the ions are periodically displaced according to equation (2). Then, the conduction electrons will try to screen the new potential and an electron density modulation of the type given in equation (1) will be created. Thus, a CDW and a PLD always come together [6, 13] (see figure 1(a)) and we will speak of a CDW/PLD throughout the paper.

A number of questions arise from this simple consideration. (i) Although a CDW and a PLD occur simultaneously, one may ask the (philosophical) chicken and egg question: which one is the driving force? In other words, is the CDW/PLD transition primarily an instability of the electron system or of the lattice? (ii) The formation of a CDW/PLD clearly costs Coulomb and elastic energy. But what are the stabilizing factors? What is the microscopic origin of a CDW/PLD? (iii) A CDW/PLD will certainly modify the electron and phonon dispersions. So what are the signatures of the CDW/PLD phase in both the electron and phonon spectra? (iv) For CDWs in one dimension and in the weak-coupling limit ($u_0/a \ll 1$) a theoretical framework is available. But can the 1D models simply be generalized to 2D? And what happens, if the coupling strength increases? In this section some answers shall be given to these questions.

2.1. Peierls instability

The Peierls instability of quasi-1D metals towards CDW/PLD formation is a consequence of strong electron–phonon

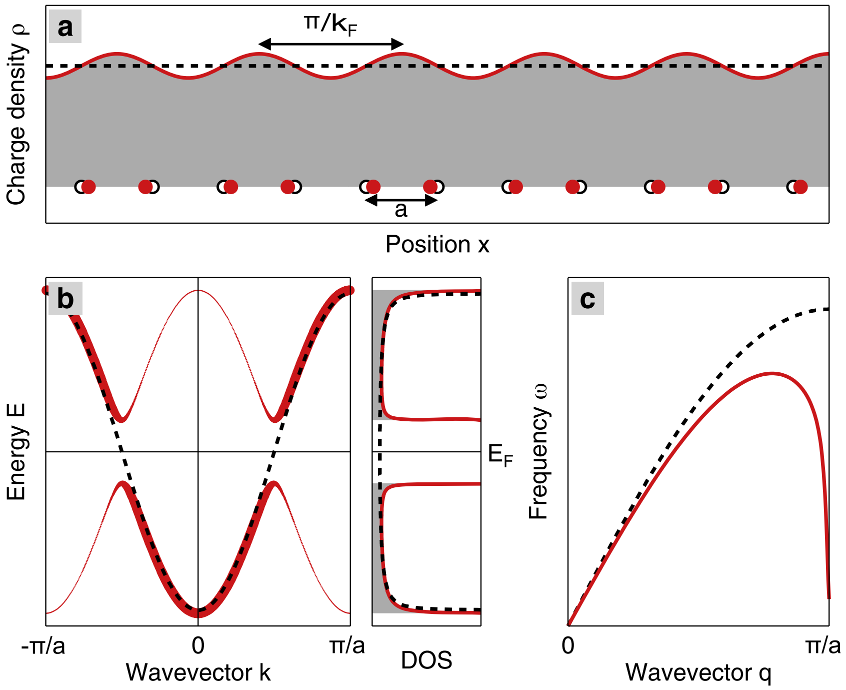

Figure 1. Peierls instability of a 1D metal with a half-filled band. (a) Schematic view of a CDW/PLD showing the modulations of the conduction electron density (solid red line) and ion positions (filled red circles). The normal state is characterized by a constant charge-density (dashed black line) and an undistorted chain (open black circles). (b) Electronic band dispersion and density of states in the metallic state above the transition temperature T_0 (dashed black lines) and in the CDW state at $T = 0$ (solid red lines). The thickness of the red lines in the band structure plot is proportional to the spectral weight carried by the electron states in the CDW phase. (c) Acoustic phonon dispersion well above T_0 (dashed black line) and at T_0 (solid red line).

interaction. The principal idea behind the Peierls model is this [1–3, 6, 25, 33]: a CDW/PLD of the type given by equations (1) and (2) sets up a potential which opens an energy gap at the Fermi surface (see figure 1(b)), thereby lowering the energy of occupied electron states and raising the energy of empty states, and since the resulting net one-electron band energy gain overcompensates the Coulomb and elastic energy cost, the CDW/PLD is self-sustaining. Note that we use the term 'Peierls instability' here to describe the instability of a coupled electron–lattice system, an instability which is, in essence, a structural phase transition driven by strong electron–phonon coupling. Thus, in contrast to other definitions [13], in this work a Peierls instability is not seen as a purely electronic phenomenon in which the lattice distortion is only an accidental by-product (see also section 2.4).

The Peierls transition to a CDW/PLD ground state can be described quantitatively by a mean-field theory of a 1D electron–lattice system in the weak-coupling limit (see, for example, [6, 19, 25, 34]). The simplest approach further implies the independent electron, harmonic and adiabatic approximations. The coupled electron–lattice system is then modeled by a Fröhlich Hamiltonian of the form

$$\begin{aligned} H_{\mathrm{PI}} = {} & \sum_{\mathbf{k}} \epsilon_{\mathbf{k}} a_{\mathbf{k}}^{+} a_{\mathbf{k}} + \sum_{\mathbf{q}} \hbar\omega_{\mathbf{q}} b_{\mathbf{q}}^{+} b_{\mathbf{q}} \\ & + \frac{1}{\sqrt{N}} \sum_{\mathbf{k},\mathbf{q}} g_{\mathbf{q}} a_{\mathbf{k}+\mathbf{q}}^{+} a_{\mathbf{k}} (b_{-\mathbf{q}}^{+} + b_{\mathbf{q}}), \end{aligned} \tag{3}$$

where $\epsilon_{\mathbf{k}}$ refers to the energy of electron state $\mathbf{k}$, $a_{\mathbf{k}}^{+}$ and $a_{\mathbf{k}}$ are the creation and annihilation operators for state $\mathbf{k}$, $\omega_{\mathbf{q}}$ is the frequency of the phonon normal mode $\mathbf{q}$, $b_{\mathbf{q}}^{+}$ and $b_{\mathbf{q}}$ are the creation and annihilation operators for phonon $\mathbf{q}$, $g_{\mathbf{q}}$ is an electron–phonon coupling constant (assumed to be independent of $\mathbf{k}$) and N is the number of lattice sites per unit length.

In this model, a static displacement $u_{\mathbf{q}}$ of phonon mode $\mathbf{q}$ sets up a potential

$$v_{\mathbf{q}} = g_{\mathbf{q}} u_{\mathbf{q}} \sqrt{\frac{2M\omega_{\mathbf{q}}}{\hbar}}, \tag{4}$$

where M is the ionic mass. The associated lattice strain energy is given by

$$\delta E_{\mathrm{lattice}} = \tfrac{1}{2} M \omega_{\mathbf{q}}^2 u_{\mathbf{q}}^2 \tag{5}$$

and the total band energy change of the electron system due to the potential $v_{\mathbf{q}}$ is (within second-order perturbation theory)

$$\delta E_{\mathrm{band}} = -|v_{\mathbf{q}}|^2 \chi_0(\mathbf{q}), \tag{6}$$

where $\chi_0(\mathbf{q})$ is the non-interacting electronic susceptibility defined as

$$\chi_0(\mathbf{q}) = \frac{1}{L} \sum_{\mathbf{k}} \frac{f_{\mathbf{k}+\mathbf{q}} - f_{\mathbf{k}}}{\epsilon_{\mathbf{k}} - \epsilon_{\mathbf{k}+\mathbf{q}}} > 0. \tag{7}$$

In this definition, $f_{\mathbf{k}}$ represents the Fermi function $f(\epsilon_{\mathbf{k}})$ and the matrix element that couples the states $\mathbf{k}$ and $\mathbf{k}+\mathbf{q}$ is, as is usually done, neglected; L is the length of the atomic chain. From equation (6) one sees that $\chi_0(\mathbf{q})$ is a direct measure of the distortion-induced band energy gain.

The new CDW/PLD ground state will be stable, if $\delta E_{\mathrm{band}} + \delta E_{\mathrm{lattice}} < 0$ for a certain phonon mode $\mathbf{q}_0$. Using equations (4)–(6), we obtain a simple instability condition for the normal state, based on microscopic parameters:

$$\frac{4g_{\mathbf{q}}^2}{\hbar\omega_{\mathbf{q}}} > \frac{1}{\chi_0(\mathbf{q})}. \tag{8}$$

Apparently, for a CDW/PLD to occur, a large electron–phonon coupling constant $g_{\mathbf{q}}$ and a large electronic susceptibility $\chi_0(\mathbf{q})$ are required at the wavevector $\mathbf{q} = \mathbf{q}_0$. By including the effects of Coulomb and exchange interactions, Chan and Heine derived a similar criterion for PLD/CDW formation [6]:

$$\frac{4g_{\mathbf{q}}^2}{\hbar\omega_{\mathbf{q}}} - 2U_{\mathbf{q}} + V_{\mathbf{q}} \geqslant \frac{1}{\chi_0(\mathbf{q})} \tag{9}$$

with the necessary hierarchy of terms:

$$\frac{4g_{\mathbf{q}}^2}{\hbar\omega_{\mathbf{q}}} > 2U_{\mathbf{q}} > V_{\mathbf{q}} > 0. \tag{10}$$

Here $U_{\mathbf{q}}$ stands for the Coulomb interaction and $V_{\mathbf{q}}$ is the screened exchange interaction. (For $4g_{\mathbf{q}}^2/\hbar\omega_{\mathbf{q}} < 2U_{\mathbf{q}}$, a spin-density wave (SDW) will set in [6].) A severe simplification implied in condition (9) is that not only $g_{\mathbf{q}}$ but also $U_{\mathbf{q}}$ and $V_{\mathbf{q}}$ are assumed to be independent of $\mathbf{k}$. Nevertheless, the criterion (9) reveals the important factors and it also confirms intuition: CDW/PLD formation is generally encouraged by strong electron–phonon and electron–electron exchange interaction (large $g_{\mathbf{q}}$ and $V_{\mathbf{q}}$), by a weak Coulomb interaction and a small lattice strain energy (small $U_{\mathbf{q}}$ and $\omega_{\mathbf{q}}$), and by a large non-interacting susceptibility (large $\chi_0(\mathbf{q})$). Beside its intuitive appeal, the instability condition (9) is also sufficiently practicable and quantitative to make contact with experimental data.

Since the CDW/PLD ground state generally occurs in systems with strong electron–phonon interactions, it can be expected that both the electron and the phonon dispersions are significantly modified upon CDW/PLD formation. In the following, we consider the archetypal situation of a 1D solid with a single half-filled band. We assume a tight-binding band dispersion

$$\epsilon_{\mathbf{k}} = -E_{\mathrm{F}}\cos(ka) \tag{11}$$

with Fermi energy E_{F} and Fermi vector $|\mathbf{k}_{\mathrm{F}}| = \pi/2a$ [34, 35]. Electron–electron interactions are again neglected ($U_{\mathbf{q}} = V_{\mathbf{q}} = 0$). For this band, when $E_{\mathrm{F}}/k_{\mathrm{B}}T$ is large, the non-interacting susceptibility at $\mathbf{q} = 2\mathbf{k}_{\mathrm{F}}$ diverges with falling temperature T as

$$\chi_0(2\mathbf{k}_{\mathrm{F}}, T) = \frac{1}{2}N(0)\ln\left(\frac{2.28E_{\mathrm{F}}}{k_{\mathrm{B}}T}\right), \tag{12}$$

where $N(0)$ is the density of electron states at the Fermi energy E_{F} (in the normal phase, per atom and including both spin directions). The sharp temperature-dependent peaking of $\chi_0(\mathbf{q}, T)$ causes a strong renormalization of the phonon frequencies in a narrow wavevector range around $\mathbf{q}_0 = 2\mathbf{k}_{\mathrm{F}}$. This is generally referred to as a giant Kohn anomaly:

$$\tilde{\omega}_{\mathbf{q}}^2 = \omega_{\mathbf{q}}^2\left(1 - \frac{4g_{\mathbf{q}}^2}{\hbar\omega_{\mathbf{q}}}\chi_0(\mathbf{q})\right), \tag{13}$$

where $\tilde{\omega}_{\mathbf{q}}$ and $\omega_{\mathbf{q}}$ denote the renormalized and normal-state phonon frequency, respectively [6]. For a non-zero electron–phonon coupling constant $g_{\mathbf{q}_0}$, we have

$$\tilde{\omega}_{\mathbf{q}_0}^2 = 0 \tag{14}$$

at a finite temperature T_0. This complete softening of phonon mode $\mathbf{q}_0$ at T_0 (see figure 1(c)) signals a phase transition to a state with a frozen-in lattice distortion, i.e. a CDW/PLD with a wavelength $\lambda_0 = 2\pi/|\mathbf{q}_0| = \pi/|\mathbf{k}_{\mathrm{F}}|$. Since $\mathbf{k}_{\mathrm{F}}$ is determined by the electron filling of the band structure in $\mathbf{k}$ space, a CDW/PLD superstructure in general will be incommensurate with the underlying crystal lattice, as opposed to the simple commensurate scenario we discuss here. Note that equations (13) and (14) lead to the simple instability criterion (8).

With equations (12)–(14), the (mean-field) transition temperature in the tight-binding approximation becomes

$$k_{\mathrm{B}}T_0 = 2.28E_{\mathrm{F}}\exp\left(-\frac{1}{\lambda}\right) \tag{15}$$

with the dimensionless electron–phonon coupling constant

$$\lambda = \frac{2g_{\mathbf{q}_0}^2 N(0)}{\hbar\omega_{\mathbf{q}_0}}. \tag{16}$$

As for the electron bands, an important point to note is that the Brillouin zone edges of the CDW/PLD superstructure characterized by $\mathbf{q}_0$ coincide exactly with the Fermi points $\pm\mathbf{k}_{\mathrm{F}}$. Thus, since the new Brillouin zone edges entail energy discontinuities, the normal-state energy band $\epsilon_{\mathbf{k}}$ splits into two branches:

$$E_{1,2}(\mathbf{k}) = \frac{\epsilon_{\mathbf{k}} + \epsilon_{\mathbf{k}+\mathbf{q}_0}}{2} \pm \sqrt{\left(\frac{\epsilon_{\mathbf{k}} - \epsilon_{\mathbf{k}+\mathbf{q}_0}}{2}\right)^2 + \Delta^2}, \tag{17}$$

separated by an energy gap 2Δ at $\mathbf{q}_0/2 = \mathbf{k}_{\mathrm{F}}$. The lower branch is completely occupied, while the upper branch is completely empty. The density of states $N(E)$ diverges at $E = \pm\Delta$ and is zero in between (see figure 1(b)), i.e. a uniform and complete energy gap opens up at E_{F}. In the model developed so far, the energy gap 2Δ is related to the displacement amplitude $u_{\mathbf{q}_0}$, the electron–phonon coupling parameter $g_{\mathbf{q}_0}$ and the unrenormalized phonon frequency $\omega_{\mathbf{q}_0}$ by [25]

$$\Delta = u_{\mathbf{q}_0}g_{\mathbf{q}_0}\sqrt{\frac{2M\omega_{\mathbf{q}_0}}{\hbar}}. \tag{18}$$

If the modified band dispersion is to be measured by ARPES, a difficulty arises from the fact that the electron states carry a $\mathbf{k}$-dependent spectral weight. The spectral weight distribution, which for a slowly varying ARPES matrix element is approximately proportional to the measured ARPES intensity distribution, is generally given by the spectral function $A(\mathbf{k}, E)$. For the modified band dispersions (17), one obtains

$$A(\mathbf{k}, E) = \frac{\delta(E - E_1(\mathbf{k}))}{1 + \frac{\Delta^2}{(E_1(\mathbf{k})-\epsilon_{\mathbf{k}+\mathbf{q}_0})^2}} + \frac{\delta(E - E_2(\mathbf{k}))}{1 + \frac{\Delta^2}{(E_2(\mathbf{k})-\epsilon_{\mathbf{k}+\mathbf{q}_0})^2}}, \tag{19}$$

where $\delta(E)$ denotes the Dirac delta function. Figure 1(b) shows that the spectral weight of the reconstructed subbands is mostly concentrated near the original band; only near $\mathbf{k}_F$, where the energy gap has opened up, are some back-bending effects observable. Thus, in contrast to the subband dispersions $E_{1,2}(\mathbf{k})$, the spectral function $A(\mathbf{k}, E)$ does not exhibit the novel periodicity of the CDW/PLD phase.

For $T = 0$ and $\Delta/E_F < 1$, it can be shown that the change in the sum of the occupied one-electron energies satisfies

$$\delta E_{\text{band}} \propto \frac{\Delta^2}{E_F} \ln\left(\frac{\Delta}{E_F}\right). \tag{20}$$

Minimization of the total energy change, $\delta E_{\text{band}} + \delta E_{\text{lattice}}$, then gives a zero-temperature energy gap (for the tight-binding band):

$$\Delta(0) = 4E_F \exp\left(-\frac{1}{\lambda}\right), \tag{21}$$

where $\lambda \lesssim 1$ [34]. Finally, with the help of equation (15), we obtain the well-known Bardeen–Cooper–Schrieffer (BCS) relation between the zero-temperature energy gap and the (mean-field) transition temperature:

$$2\Delta(0) = 3.52 k_B T_0. \tag{22}$$

Although the picture presented through the above equations is that of a full microscopic theory, it has to be pointed out that this theory has many weaknesses connected with the various approximations made. For example, the mean-field solution of the 1D model neglects the effects of fluctuations and predicts long-range order at a finite transition temperature, which can in fact only come about when the system is quasi-1D, i.e. when there is some finite coupling between neighboring chains [25]. Also, within the independent electron approximation, it turns out that a Peierls instability will always occur at a low enough temperature, while, if electron–electron interactions are included, the 1D metal may indeed be stable [36]. In the next two sections, we briefly summarize what happens when the assumptions of weak coupling and one dimensionality are relaxed.

2.2. Weak coupling versus strong coupling

When the electron–phonon coupling strength is increased, the physics of CDW/PLD formation does not change fundamentally, but most of the formulae given above cannot be applied anymore. Compared to a weak-coupling CDW, a strong-coupling CDW is characterized by a larger distortion amplitude, a larger energy gap and a smaller coherence length as, for example, given by the inverse width of the Kohn anomaly in the $\omega(\mathbf{q})$ diagram. The dividing line between the two is roughly set by the ratio $\Delta/\hbar\omega_D \approx 1$ (with the electronic energy gap Δ and the Debye phonon frequency ω_D) [30, 37].

In both cases, the origin of the energy gain is electronic. However, for a small energy gap ($\Delta/E_F \ll 1$), the band energy gain originates mostly near $\mathbf{k}_F$ and is of order $\Delta^2 \ln \Delta$ (equation (20)), whereas for a large gap ($\Delta/E_F \lesssim 1$), the energy gain is spread over the entire Brillouin zone and proportional to Δ [38]. Hence, the relative importance of the Fermi surface for CDW/PLD formation is reduced as the coupling strength is increased.

The thermodynamic behavior near the transition temperature T_0 is also markedly different [38, 39]. In a weak-coupling CDW, the thermal disordering is dominated by electronic entropy, arising from electronic excitations across the gap, and above T_0 the CDW/PLD vanishes completely. In a strong-coupling CDW, on the other hand, the transition is driven by the entropy of the lattice and only the long-range coherence of the CDW/PLD is lost at T_0. Above T_0, fluctuating short-range distortions remain and it is expected that these fluctuations smear, but do not destroy, the energy gap and cause strong carrier scattering [39]. The undistorted state will finally be restored at a temperature well above T_0.

In McMillan's (2D) microscopic model of strong-coupling/short-coherence-length CDW/PLDs [39], the (normal metal-to-incommensurate CDW) transition temperature is given by

$$k_B T_0 = 0.296 C \frac{(\pi \xi_0 u_0)^2}{2\Omega}, \tag{23}$$

where ξ_0 is the coherence length, u_0 the distortion amplitude, Ω the area of the normal-state unit cell and C (in eV Å^{-2}) a measure for the electron–lattice coupling. This equation is to be compared to equation (15) for the weak-coupling CDW/PLD transition temperature (in 1D). Quite generally, it can be expected that strong coupling will lead to significant deviations from the BCS equation (22), i.e. $2\Delta(0) > 3.52 k_B T_0$.

It has been suggested that in the extreme limits of weak and strong coupling two qualitatively different pictures apply [38, 39]. In the long-coherence-length picture, the CDW/PLD transition can be understood in terms of the Peierls instability. As shown above, this instability is intimately connected with the Fermi surface and thus deeply rooted in $\mathbf{k}$ space, where long-range order and incommensurability are easily explained. In the short-coherence-length picture, on the other hand, a local-chemical-bonding picture is often more appropriate [24, 39–41]. Due to the much larger atomic displacements, nonlinear terms in the electron–lattice interaction are important. The atoms then show a tendency to form pairs with shortened bonds as well as clusters and the CDW/PLDs tend to lock into the underlying crystal lattice. It should be pointed out that the two seemingly different pictures are just two sides of the same coin, because one can pass continuously from one limit to the other [38]. The complementarity is also reflected in the common analogy between the Peierls instability in low-dimensional solids and the Jahn–Teller effect in molecules [33].

A theory for the intermediate-coupling regime is presently not available [42], but it can be expected that looking at both the electronic structure in $\mathbf{k}$ space and the local chemical bonding in real space may help to understand intermediately coupled CDWs. Table 1 summarizes the different properties of weak-coupling and strong-coupling CDWs.

2.3. One dimension versus two dimensions

Dimensionality has a profound effect on two important factors in the standard theory of CDW/PLD formation: on the peaking

Table 1. Qualitative comparison of weak-coupling and strong-coupling CDWs.

	Weak-coupling CDW	Strong-coupling CDW
PLD/CDW amplitude	Small	Large
Energy gap	Small ($\Delta/E_F \ll 1$)	Large ($\Delta/E_F \lesssim 1$)
Coherence length	Large ($\xi/a \gg 1$)	Small ($\xi/a \gtrsim 1$)
Electronic energy gain	Arising mostly near k_F ($\propto\Delta^2 \ln \Delta$)	Spread over Brillouin zone ($\propto\Delta$)
CDW periodicity w.r.t. original lattice	Incommensurate ($\lambda_0 = \pi/k_F$)	Tends to be commensurate
Thermal disordering	Due to electronic entropy	Due to lattice entropy
Electron–hole pairing above T_0	No	Yes, but pairs are incoherent
Qualitative picture	Fermi surface instability	Local chemical bonding

of the non-interacting susceptibility $\chi_0(\mathbf{q})$ and on the flatness of the Fermi surface $\epsilon_\mathbf{k} = E_F$.

In one dimension, it is the logarithmic divergence of $\chi_0(\mathbf{q}_0)$ with falling temperature (equation (12)) that drives the CDW/PLD transition. It causes the phonon mode $\mathbf{q}_0$ to soften completely and it ensures a large band structure energy gain to be made. The wavevector of the singularity becomes the wavevector of the CDW/PLD superstructure. However, as pointed out recently [13], the logarithmic divergence of the non-interacting susceptibility is not particularly robust against temperature, lifetime and momentum broadening effects. Note that momentum broadening naturally arises in quasi-1D systems, in which interchain interactions lead to a buckling of the Fermi surface. Consider then the enhancement $\chi_0(\mathbf{q}_0)/\chi_0(0)$, which is infinite for the ideal 1D case at $T = 0$. For realistic parameters ($E_F = 0.3$ eV, $|\mathbf{k}_F| = 0.5$ Å^{-1}), the infinite enhancement is easily reduced to a factor of only about three for, respectively, a temperature of 200 K, an energy broadening of 5 meV or a momentum broadening of 0.01 Å^{-1} [13]. Thus, in realistic situations a sufficiently large electron–phonon coupling $g_{\mathbf{q}_0}$ is absolutely necessary for a CDW/PLD transition to occur (see equation (8)).

What is the role of the Fermi surface with respect to the CDW/PLD transition in 1D? Looking at definition (7), a large $\chi_0(\mathbf{q})$ requires a large numerator $f_{\mathbf{k}+\mathbf{q}} - f_\mathbf{k}$, a small denominator $\epsilon_\mathbf{k} - \epsilon_{\mathbf{k}+\mathbf{q}}$ and many such $\mathbf{q}$-coupled states, i.e. a high density of states. The largest contribution to $\chi_0(\mathbf{q})$ is expected to arise near the Fermi surface. In the weak-coupling limit, indeed, this is the case. But even then, electronic states away from $\mathbf{k}_F$ (in the entire Brillouin zone) are not negligible as the factor $\ln(\Delta/E_F)$ in equation (20) is known to originate particularly from such states [13, 37]. When the coupling strength is increased, the electronic energy gain cannot be easily localized in $\mathbf{k}$ space anymore and the role played by the Fermi surface effectively tends to zero.

For a 2D metal, the situation becomes even worse because $\mathbf{k}$-space geometry is generally not favorable. In 3D $\mathbf{k}$ space, a 1D metal has a planar Fermi surface which can exactly coincide with the planar energy discontinuities created by the CDW/PLD, thus resulting in a uniform and complete energy gap at the Fermi level ($N(0) = 0$). For a 2D metal, on the other hand, the Fermi surface is generally not planar so that the new Brillouin zone edges will only partly coincide with the Fermi surface. The energy gap is then also only partial ($N(0) > 0$). The best case scenario occurs when the Fermi surface is effectively 1D, i.e. when it has large flat parallel sections. The resulting possibility to displace one section of the Fermi surface by a single wavevector $\mathbf{q}$ and to superimpose it exactly onto another section is the well-known concept of Fermi surface nesting, which, however, may only be used for a simple qualitative analysis of the electronic response in higher dimensions [13].

The effect of dimensionality on the form of the non-interacting electronic susceptibility is dramatic. Upon the transition from perfect ($D = 1$) to weak ($D > 1$) Fermi surface nesting, the logarithmic divergence evolves into a smooth peak whose height and position critically depend on the size and curvature of the nested Fermi surface segments [43]. We note that, apart from Fermi surface nesting, significant contributions to $\chi_0(\mathbf{q})$ can also arise in two dimensions from the nesting of saddle points in the band structure, if the saddle points are very close to E_F [44]. In general, however, layered CDW materials are notoriously known for showing only a weak peaking of $\chi_0(\mathbf{q})$ in a rather broad wavevector range around the experimentally observed $\mathbf{q}_0$ [13, 23, 45–48]. The Kohn anomalies are therefore smaller and broader than in 1D materials and, consequently, the electron–phonon coupling required for the occurrence of a CDW/PLD is larger [25, 49]. Also, in 2D systems the temperature dependence of $\chi_0(\mathbf{q})$ is generally very weak [23, 46].

In two dimensions, yet another problem arises. If the Fermi surface is anisotropic, the $\mathbf{k}$ dependence of the electron–phonon matrix element cannot be neglected anymore and the simple instability criteria (8) and (9) cease to be valid. The expression for the electronic susceptibility has to be generalized to

$$\chi(\mathbf{q}) = \frac{1}{L}\sum_{\mathbf{k}} |g'_{\mathbf{k},\mathbf{k}+\mathbf{q}}|^2 \frac{f_{\mathbf{k}+\mathbf{q}} - f_\mathbf{k}}{\epsilon_\mathbf{k} - \epsilon_{\mathbf{k}+\mathbf{q}}}, \tag{24}$$

where $g'_{\mathbf{k},\mathbf{k}+\mathbf{q}}$ denotes the $\mathbf{k}$-dependent electron–phonon matrix element. As a rule of thumb, $g'_{\mathbf{k},\mathbf{k}+\mathbf{q}}$ is large when $\mathbf{k}$ and $\mathbf{k} + \mathbf{q}$ are states with large and opposite band velocities [50]. In layered CDW systems, the electron–phonon matrix element depends rather strongly on $\mathbf{k}$ [23, 48, 51], but in most cases it does not become dominant in $\chi(\mathbf{q})$: the peaking of $\chi(\mathbf{q})$ is more pronounced than the peaking of $\chi_0(\mathbf{q})$; still, it is not sharp enough to pick out the correct $\mathbf{q}_0$ [23, 48, 52].

In a nutshell, when going from one dimension to two dimensions, the role of the electronic susceptibility in CDW/PLD formation appears to be largely diminished, and the same holds for the role of the Fermi surface. Our qualitative comparison of 1D and 2D CDW systems is summarized in table 2.

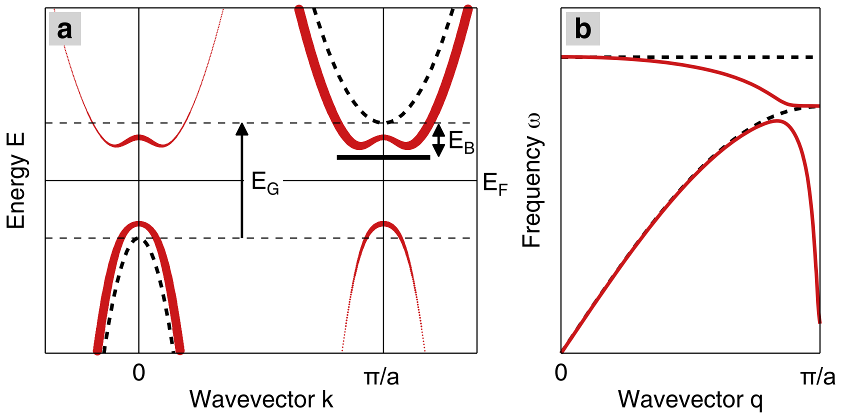

Figure 2. Excitonic insulator instability of a semiconductor with a small indirect bandgap. (a) Electronic band dispersion in the normal phase (dashed black lines) and in the excitonic insulator phase (solid red lines), after the bandgap E_G has become smaller than the binding energy of the exciton state E_B. The thickness of the red lines is proportional to the spectral weight carried by the electron states in the excitonic insulator phase. (b) Exciton and phonon dispersions in the normal phase (dashed black lines) and in the excitonic insulator phase (solid red lines). In the depicted situation, the soft (spin singlet) exciton mode interacts strongly with a phonon mode.

Table 2. Qualitative comparison of ideal 1D and 2D metals with respect to CDW/PLD formation.

	1D	2D
Fermi surface:		
Geometry (in 3D)	Planar	Cylindrical
Nesting	Perfect	Weak
Electronic susceptibility:		
$\mathbf{q}$ dependence ($T = 0$)	Log. divergence	Weak peaking
T dependence ($\mathbf{q} = \mathbf{q}_0$)	Log. divergence	Weak peaking
Kohn anomaly	Large, sharp	Small, broad
$g_{\mathbf{q}}$ required for CDW	Small	Large
CDW energy gap	Complete	Partial

2.4. Excitonic insulator instability

Up to this point, we have discussed a situation with a single metallic band and a CDW/PLD transition driven by an electron–phonon interaction. Now, we consider a two-band model with a small indirect bandgap/overlap and a 'pure' CDW transition that is driven by an electron–electron interaction—the so-called excitonic insulator instability [4, 5].

Let us assume a valence band with maximum at $\mathbf{k} = 0$ and a conduction band with minimum at $\mathbf{k} = \mathbf{q}_0$:

$$\epsilon^a_{\mathbf{k}} = -\frac{1}{2}E_G - \frac{\hbar^2}{2m_a}\mathbf{k}^2, \qquad \epsilon^b_{\mathbf{k}} = \frac{1}{2}E_G + \frac{\hbar^2}{2m_b}(\mathbf{k} - \mathbf{q}_0)^2, \tag{25}$$

where E_G is the energy gap, and m_a and m_b are effective masses, and let us consider qualitatively what may happen at the semiconductor ($E_G > 0$)-to-semimetal ($E_G < 0$) transition, when the Coulomb interaction is taken into account (see figure 2). First, we start on the semiconducting side with an energy gap $E_G > E_B > 0$, where E_B is the binding energy of the lowest-lying excitons, and reduce E_G by some external parameter. During this process, E_B is expected to remain finite such that eventually a point can be reached at which the exciton excitation energy $E_G - E_B$ goes to zero. Then, an electronic instability occurs due to the spontaneous formation of excitons. Similarly, if we start with a semimetal with a small band overlap $|E_G|$, the excitation energy of a plasmon can go to zero when the band overlap becomes smaller than some critical energy $|E_1|$ ($E_1 < 0$). This instability can be connected to screening effects. If the number of electrons and holes in the semimetal becomes sufficiently small, the Coulomb attraction between them will be insufficiently screened so that bound states are formed, turning the semimetal into an insulator. Taken together, the normal insulating and semimetallic ground states are unstable in the range $E_1 < E_G < E_B$ [4, 5].

Besides the complete softening of an exciton or plasmon mode, the excitonic insulator state is signaled by the formation of an electron density wave as well as by changes to the band structure, and possibly by a lattice distortion. Depending on the total spin S of the soft mode, the superstructure in the electron density can be an antiferromagnetic SDW, for $S = 1$, or a CDW, for $S = 0$. In both cases, the density oscillation will have the wavelength $\lambda_0 = 2\pi/|\mathbf{q}_0|$. In the case of the SDW, the soft electronic mode does not interact with the phonon modes of the system so that the lattice period will not be modulated. For the CDW, on the other hand, strong mixing between the soft electronic mode and some phonon mode (both having $S = 0$) will generally occur (see figure 2(b)) and the CDW will be accompanied by a PLD with the same periodicity. In a strict sense, this CDW/PLD is in contrast to the one resulting from the Peierls instability, which is an instability of the combined electron–lattice system driven by strong electron–phonon coupling. The excitonic insulator instability is primarily an electronic instability, the driving force is the electron–electron interaction (electron–hole attraction) and the lattice distortion is therefore only a by-product resulting from a finite electron–phonon coupling. It should be pointed out, however, that although the driving force may be different the outcome of Peierls and excitonic insulator instabilities is qualitatively the same: a novel ground state with broken translational symmetry exhibiting a CDW, a PLD and a gap in the one-electron spectrum. Moreover, the two scenarios are mathematically indistinguishable [53] (see table 3 for a qualitative comparison).

Table 3. Qualitative comparison of two basic CDW mechanisms: Peierls instability versus excitonic insulator instability.

	Peierls instability	Excitonic insulator
Type of instability	Electron + lattice	Primarily electronic
Archetypal situation	1 band, odd valence	2 bands, even valence
Dominant interaction	Electron–phonon	Electron–hole
Type of density wave	CDW/PLD	CDW (SDW)
Soft collective mode	Phonon	Exciton or plasmon
Lattice distortion	Large	Small (none)

The modification of the electronic band structure in the excitonic insulator phase can be modeled by the simple effective Hamiltonian (cf equation (3)):

$$H_{\mathrm{EI}} = \sum_{\mathbf{k}} \epsilon^a_{\mathbf{k}} a^+_{\mathbf{k}} a_{\mathbf{k}} + \sum_{\mathbf{k}} \epsilon^b_{\mathbf{k}} b^+_{\mathbf{k}} b_{\mathbf{k}} + \sum_{\mathbf{k}} \Delta_{\mathbf{k}} \left(b^+_{\mathbf{k}} a_{\mathbf{k}} + a^+_{\mathbf{k}} b_{\mathbf{q}} \right). \tag{26}$$

Via the last term, states in the valence and conduction band—separated in wavevector by $\mathbf{q}_0$—are connected. If we set $\Delta = \Delta_{\mathbf{k}} = \text{const.}$, $\epsilon_{\mathbf{k}} = \epsilon^a_{\mathbf{k}}$ and $\epsilon_{\mathbf{k}+\mathbf{q}_0} = \epsilon^b_{\mathbf{k}+\mathbf{q}_0}$, we can reuse equations (17) and (19) for the reconstructed band structure and the spectral function, respectively. Figure 2(a) illustrates the effects. The valence and conduction band parabolae are mapped onto each other, the band edges become repelled and some spectral weight is transferred from the original bands to the reconstructed ones. The nature of the resulting state depends on the sign of the gap E_{G} and on whether the two bands $\epsilon^a_{\mathbf{k}}$ and $\epsilon^b_{\mathbf{k}}$ have the same or different anisotropies (in the k_x and k_y direction). When E_{G} is positive, the resulting band scheme will always be that of an insulator. If, on the other hand, E_{G} is originally negative, an insulating ground state occurs only when the band anisotropies are the same. For different band anisotropies, the modified bands will overlap and the new ground state will be semimetallic [4].

2.5. Application to real materials

Before we turn from the theoretical background to the review of the properties of the selected CDW/PLD materials, we may ask whether the presented models can indeed be applied to real materials.

As for the Peierls instability, as detailed in section 2.1, the model with its formulae certainly helps to identify and understand, at least semi-quantitatively, CDW/PLD transitions in real materials, in particular in quasi-1D solids [25]. It can also be seen as a reasonable starting point for more sophisticated microscopic theories. The theory of the Peierls instability is, however, based on weak coupling and special (1D) features of the near-E_{F} electronic structure and is therefore expected to become inappropriate when the electron–phonon coupling and energy gapping are large and Fermi surface geometry is not 1D-like. Nevertheless, when realistic calculations are not available, the Peierls model provides a theoretical framework within which semi-quantitative predictions can be compared with experimental data. In section 5, we shall take this approach for the selected layered CDW/PLD systems.

Concerning the model of the 'pure' excitonic insulator instability, its relevance for real materials is less clear. In real materials, electron–phonon coupling and electron–hole attraction are always simultaneously present such that the classification of a system as either a Peierls insulator or an excitonic insulator is generally ambiguous. (Note that in the Chan–Heine condition (9), which will frequently be used in our analysis of the CDW/PLDs in the layered compounds, the presence of the two interactions is indicated by the parameters $g_{\mathbf{q}}$ and $V_{\mathbf{q}}$.) It is nevertheless surprising that, while the existence of Peierls insulators is undoubted, there are only a few materials for which experimental evidence for an excitonic insulator state has been reported. Two important examples are the rare earth compound $\mathrm{TmSe_{0.45}Te_{0.55}}$ [54] and the layered transition-metal compound 1T-$\mathrm{TiSe_2}$ [11]. For the latter material, whose electronic structure is so suggestive of the excitonic insulator instability, we will specifically investigate in section 4 whether evidence can be found for a strong excitonic contribution to the observed electronic structure changes.

3. CDW/PLDs in the layer compounds 1T-$\mathrm{TaS_2}$, 2H-$\mathrm{TaSe_2}$ and 1T-$\mathrm{TiSe_2}$

For our study of CDW/PLD formation in the family of layered transition-metal dichalcogenides, we select here 1T-$\mathrm{TaS_2}$, 2H-$\mathrm{TaSe_2}$ and 1T-$\mathrm{TiSe_2}$ from the nine family members that are known to undergo a transition to a CDW/PLD state (only pure compounds and 1T, 2H and 4H$_b$ polytypes counted [18]). These three compounds are perhaps the most extensively studied ones and they are especially characterized by high transition temperatures, well above 77 K, that lead to significant and reproducible effects upon CDW/PLD formation. Besides having large amplitudes, the CDW/PLDs in 1T-$\mathrm{TaS_2}$, 2H-$\mathrm{TaSe_2}$ and 1T-$\mathrm{TiSe_2}$ are also remarkably robust against imperfection as they survive transition-metal or chalcogen substitution up to the 15% level [18, 55, 56], intercalation of metal atoms up to the 5% level [9, 57] and alternating octahedral (1T) and trigonal prismatic (2H) coordination as in the 4H$_b$ Ta compounds [18, 58–60]. One may therefore expect that these CDW/PLDs can be more easily linked to a specific mechanism. On the other hand, strong effects naturally imply that one leaves the solid framework of weak-coupling theory. The basic undistorted crystal structures of the 1T and 2H polytypes are illustrated in figure 3.

3.1. Summary of observed CDW/PLD phases

We begin this brief review with 1T-$\mathrm{TaS_2}$, the compound with the richest phase diagram of all transition-metal dichalcogenides. If we start at roughly 560 K and lower the temperature, a sequence of CDW/PLD phases with some kind of ordering close to a $\sqrt{13} \times \sqrt{13}$ superstructure will occur [18, 61]. The CDW/PLD is incommensurate between 543 and 352 K, nearly commensurate from 352 to 183 K (from 221 to 355 K upon heating), and finally commensurate below 183 K [18, 59, 61]. The incommensurate, nearly commensurate and commensurate phases are also called 1T$_1$, 1T$_2$ and 1T$_3$, respectively. On the way from the incommensurate to the commensurate phase, the rotation

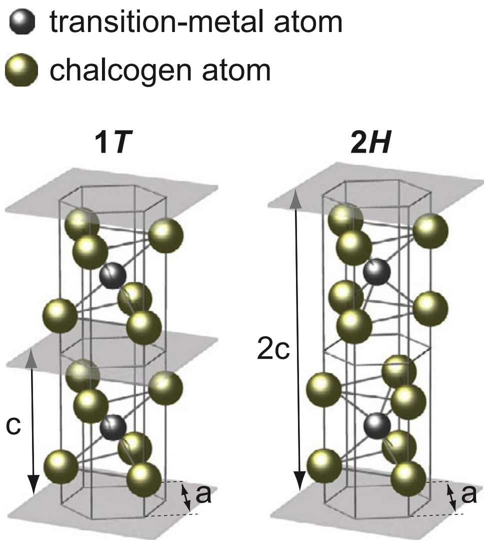

Figure 3. Schematic crystal structure of the 1T (left) and the 2H (right) polytype of layered transition-metal dichalcogenides. In the 1T structure, the transition-metal atoms are octahedrally coordinated by chalcogen atoms and the thickness of the repeat unit in the *c* direction is one sandwich. In the 2H structure, the coordination is trigonal prismatic and the unit cell is two sandwiches thick.

angle of the superlattice with respect to the undisturbed lattice changes from 0° to 13.9° [61]. In the nearly commensurate phase, the rotation angle is about 12° ± 1°. In this phase, commensurate domains are present, arranged in a hexagonal 'super-superlattice' and separated by discommensurate areas [63]. In the commensurate phase, the Ta atoms are grouped into 13-atom clusters with a 'Star-of-David' arrangement, as shown in figure 4 (left). The Ta atom displacements are very large, up to 0.24 Å, and mostly in-plane. The displacements of the S atoms are smaller by about a factor of two and mostly out-of-plane [62]. As to a possible out-of-plane periodicity of the CDW/PLD, it can be noted that the stacking sequence of the Ta layers has a period of three in the incommensurate and nearly commensurate phases [61], but that it is not clear whether the stacking sequence is disordered [64–66] or has a period of 13 [63] in the commensurate phase.

A distinctive feature of the (first-order) nearly commensurate–commensurate phase transition in 1T-TaS$_2$ is that electron correlation effects are involved. In the presence of the commensurate CDW/PLD, the electronic states in the partially filled Ta 5d band are regrouped such that a Mott–Hubbard transition can occur, to a state with overlapping Hubbard subbands and thus a pseudogap at the Fermi level [67]. The few remaining states at E_F are then sensitive to Anderson localization, which is finally responsible for the observed semiconducting behavior of commensurate phase 1T-TaS$_2$ [68]. A CDW phase with semiconducting properties is the exception in the family of transition-metal dichalcogenides. All other CDW phases are metallic or even superconducting at low temperatures.

Compared to 1T-TaS$_2$, the phase diagram of 2H-TaSe$_2$ is less complex. Upon cooling, 2H-TaSe$_2$ undergoes a second-order transition at 122 K to an incommensurate phase with a modulation close to a 3 × 3 reconstruction, which is followed by a first-order lock-in transition at 90 K to the commensurate 3 × 3 state [69]. Upon warming, a 'striped' incommensurate phase with broken hexagonal symmetry has also been found between 93 and 112 K [70]. In the commensurate phase, the Ta atoms form seven-atom clusters, similar to the inner seven atoms of the 'Stars of David' in 1T-TaS$_2$ [62] (figure 4 (middle)). At a temperature of 5 K, the in-plane Ta atom displacements are about 0.05 Å, more than five times larger than the in-plane Se atom displacements [69]. As in 1T-TaS$_2$, the movements of the chalcogen atoms in the perpendicular direction, into the van der Waals gaps between the Se–Ta–Se sandwiches, are slightly more pronounced.

Compared to the two Ta compounds, the CDW/PLD transition in 1T-TiSe$_2$ is markedly different: a commensurate superlattice forms without the occurrence of an incommensurate phase, the transition involves a wavevector corresponding to a high-symmetry point of the Brillouin zone and the CDW/PLD undoubtedly shows 3D long-range ordering. At 202 K, 1T-TiSe$_2$ undergoes a second-order phase transition to a commensurate 2 × 2 × 2 CDW/PLD [71]. The atomic displacement pattern within an Se–Ti–Se sandwich is shown in figure 4 (right). At low temperature (77 K), the metal atom displacements are again quite large, about 0.085 Å, and the ratio of Ti to Se displacements is 3:1 [71].

All three compounds develop a triple-**q** CDW, i.e. the charge-density modulation is given by

$$\rho(\mathbf{r}) = \rho_0(\mathbf{r}) \left[1 + \sum_{i=0}^{2} \rho_i \cos(\mathbf{q}_i \mathbf{r} + \phi_i) \right], \qquad (27)$$

where $\rho_0(\mathbf{r})$ describes the unperturbed electron density, and ρ_i, $\mathbf{q}_i$ and ϕ_i are the amplitudes, wavevectors and phases of the three superimposed electron density modulations (cf equation (1)). In the commensurate CDW phases, the CDW wavevectors can be expressed as linear combinations of the hexagonal reciprocal lattice vectors $\mathbf{a}_i^*$ ($i = 0, 1, 2$): $\mathbf{q}_0 = \frac{1}{13}(3\mathbf{a}_0^* + \mathbf{a}_1^*)$ or $\mathbf{q}_0' = \frac{1}{13}(-3\mathbf{a}_0^* + 4\mathbf{a}_1^*)$ for 1T-TaS$_2$ (in-plane components only), $\mathbf{q}_0 = \frac{1}{3}\mathbf{a}_0^*$ for 2H-TaSe$_2$ and $\mathbf{q}_0 = \frac{1}{2}(\mathbf{a}_0^* + \mathbf{a}_2^*)$ for 1T-TiSe$_2$. The wavevectors $\mathbf{q}_1$ and $\mathbf{q}_2$ are in each case obtained by rotating $\mathbf{q}_0$ around the k_z axis by ±120°. Figure 4 shows the projected real-space unit cells and Brillouin zones for the three materials.

In the following, we will only be concerned with the microscopic origin of the transition from a normal undistorted phase to a (commensurate) CDW/PLD phase and not with the various transitions between incommensurate, nearly commensurate and commensurate CDW/PLD phases. The latter have been successfully modeled by phenomenological Landau theory [72, 73].

3.2. Characteristics of the CDW/PLD states

Beginning in the mid-1970s [18], a broad variety of experimental and theoretical studies have been performed on 1T-TaS$_2$, 2H-TaSe$_2$ and 1T-TiSe$_2$. The experimental techniques used include x-ray, neutron and electron scattering to determine structural changes and angle-resolved photoemission, scanning

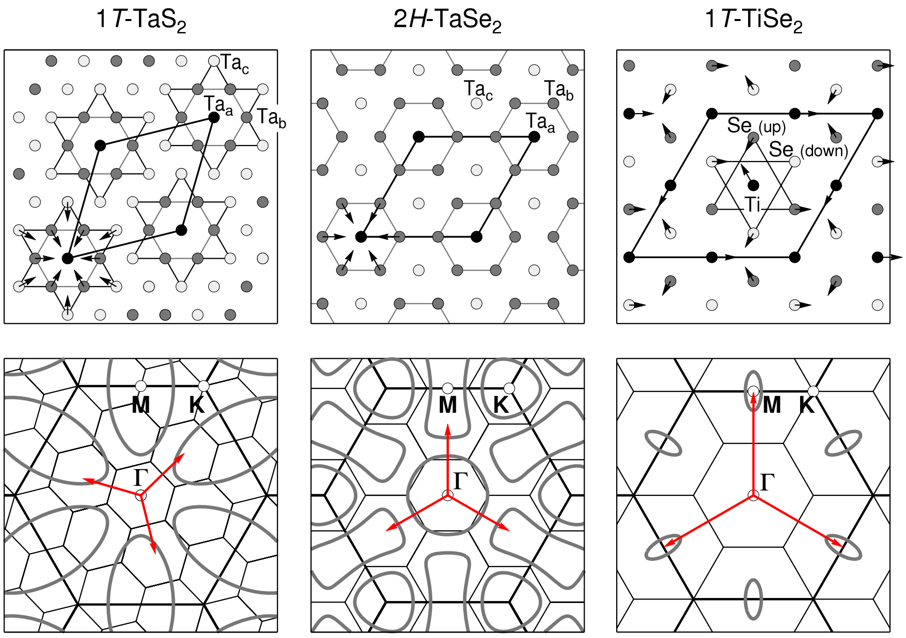

Figure 4. Real-space unit cells (top) and Brillouin zones (bottom) for the commensurate $\sqrt{13} \times \sqrt{13}$ (left), 3×3 (middle) and 2×2 (right) superlattices within a single sandwich layer of 1T-TaS$_2$, 2H-TaSe$_2$ and 1T-TiSe$_2$, respectively. In the top row, the arrows indicate in-plane displacements of the atoms from their original positions (arrow lengths are not to scale). For 1T-TaS$_2$ and 2H-TaSe$_2$ only the Ta atoms are shown; there are inequivalent 'a', 'b' and 'c' Ta atomic sites in the distortion patterns. In the bottom row, the red arrows indicate the in-plane wavevectors of the various CDWs and the gray contours illustrate the topology of the equi-energy contours near the Fermi energy for the transition-metal d-derived states in the normal phase.

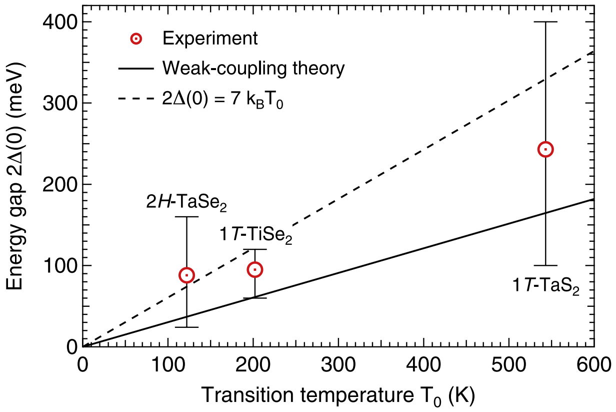

Figure 5. Experimentally determined energy gap sizes (open symbols) versus CDW/PLD transition temperatures for 2H-TaSe$_2$, 1T-TiSe$_2$ and 1T-TaS$_2$. For comparison, the prediction of weak-coupling theory (solid line) and a heuristic criterion for the applicability of the strong-coupling limit (dashed line) are also indicated.

tunneling and optical spectroscopy as well as specific heat and transport measurements to characterize the electronic properties and the changes in the electronic spectrum. On the theoretical side, density-functional theory within the local density approximation (LDA) has provided quite accurate results on the electronic structure near the Fermi level, at least for the unreconstructed phases. Table 4 summarizes selected experimental and theoretical results. From these, a number of conclusions can be drawn.

(i) First of all, there is strong evidence for the occurrence of a CDW/PLD transition in all three compounds because in each case the presence of the three most important signatures—a periodic lattice distortion and an energy gap below a certain transition temperature and a Kohn anomaly above that temperature—is consistent with the experimental data.

(ii) For all three systems, the electron–phonon coupling is strong, as can be concluded from several experimental results. First, the amplitudes of the PLDs are large; for the maximum displacement of the transition-metal atoms relative to the lattice constant one finds $u_{\max}/a = 1.5$–7%. Second, the depression of the phonon frequency at the CDW/PLD wavevector due to the Kohn anomaly appears to be significant: $1 - \omega_{\mathbf{q}_0}/\omega_{\mathbf{q}_{\max}} \approx 0.2$–0.7, where $\omega_{\mathbf{q}_{\max}}$ is the maximum phonon frequency in the branch that shows the softening. And, third, although there is some uncertainty about the precise values, the average experimental energy gaps in the electronic spectra are large, both with respect to the Fermi energy and the transition temperature: $\langle 2\Delta(0)\rangle/E_F \approx 0.15$–0.5 and $\langle 2\Delta(0)\rangle/k_B T_0 = 5.56 \pm 1.20 \gtrsim 3.52$ (see figure 5). (The average experimental energy gaps $\langle 2\Delta(0)\rangle$ are 243 ± 113 meV (1T-TaS$_2$), 88 ± 53 meV (2H-TaSe$_2$) and 95 ± 25 meV (1T-TiSe$_2$).) Large energy gapping is also indicated by a significant reduction of the density of states at the Fermi level: $N(0)^*/N(0) < 0.5$, where $N(0)^*$ denotes the low-temperature value derived from specific heat measurements and $N(0)$ comes from band structure calculations performed for the undistorted phases. For the

Table 4. Selected experimental and theoretical parameters for the layered CDW compounds 1T-TaS$_2$, 2H-TaSe$_2$ and 1T-TiSe$_2$.

	1T-TaS$_2$	2H-TaSe$_2$	1T-TiSe$_2$
Transition temperatures			
T_{ICDW} (K)	543[a]	122[b]	—
T_{CCDW} (K)	183–221[a]	90[b]	202[c]
Lattice distortion			
Superstructure	$\sqrt{13} \times \sqrt{13}$[d]	3×3[b]	$2 \times 2 \times 2$[c]
Displacement $u_{\max}/a$	7%[e]	1.5%[f]	2.4%[c]
Energy gap			
$2\Delta(0)$ (meV)	100–400[g]	24–160[h]	60–120[i]
Kohn anomaly[j]			
$\hbar\tilde{\omega}_{\mathbf{q}_0}$ (meV)	4.8[k]	7.0[b]	5.4[l]
$1 - \tilde{\omega}_{\mathbf{q}_0}/\tilde{\omega}_{\mathbf{q}_{\max}}$	73%[k]	22%[b]	42%[l]
$\lvert\mathbf{q}_0 - \mathbf{q}_{\max}\rvert$ (Å^{-1})	0.32[k]	0.26[b]	0.44[l]
LDA band structure			
E_{F} (eV)	∼1.3[m]	∼0.6[n]	∼0.2[n]
$N(0)$ (states/eV u.c.)	1.4–1.7[o]	5.2[o]	0.9–1.5[p]
Specific heat			
$N(0)^*$ (states/eV u.c.)	0.2–0.6(1.8)[q]	1.9–2.2[r]	0.08[s]
Θ_{D} (K)	249[q]	201[r]	251[s]
Electrical resistivity			
ρ (mΩ cm)[t]	∼0.2[u]	∼0.1[v]	∼1[w]
$\rho_\perp/\rho_\parallel$	∼500[x]	∼25[v]	∼2.5[w]
Lattice constants[y]			
a (Å)	3.365	3.435	3.536
c (Å)	5.883	2×6.359	6.004

[a] Thermal and transport measurements [59].
[b] Neutron scattering [69]. [c] Neutron scattering [71].
[d] Electron diffraction [18]. [e] X-ray diffraction [62].
[f] Neutron scattering [69, 74].
[g] ARPES, scanning tunneling spectroscopy, optical conductivity and tight-binding simulations [75–79]. The value range does not necessarily reflect the size of the CDW gap because below ≈180 K there is also a Mott–Hubbard-type gap.
[h] ARPES, scanning tunneling spectroscopy and optical spectroscopy [80–85].
[i] ARPES [11, 86–89]. [j] Near room temperature.
[k] X-ray thermal diffuse scattering at 360 K [90].
[l] X-ray thermal diffuse scattering at 295 K [91].
[m] Reference [92]. [n] For a semimetallic normal phase [93].
[o] Reference [94] and references therein.
[p] Reference [95] and references therein.
[q] References [18, 96]. [r] References [18, 97].
[s] Reference [98]. [t] Above T_{CDW}. [u] At 550 K [12].
[v] At 300 K [99]. [w] At 300 K [71]. [x] Reference [100].
[y] Average values from references compiled in [101].

strong-coupling limit to apply, it has been suggested [39] that $2\Delta(0)/k_{\mathrm{B}}T_0 > 7$. As can be seen in figure 5, the measured gap sizes place the three materials somewhere in the intermediate to strong-coupling regime.

(iii) A strong interaction between electrons and phonons is also suggested by the relatively high electrical resistivity above the transition temperature. For all three compounds, $\rho \geqslant 0.1$ mΩ cm, which is roughly 50 times larger than the resistivity of Cu at 373 K [102]. Such high carrier scattering rates above T_0 have been interpreted as being caused by fluctuations of a strong-coupling CDW/PLD [103].

(iv) Using the inverse width of the Kohn anomaly $1/|\Delta\mathbf{q}|$ as a measure for the coherence length, we obtain $\pi/|\Delta\mathbf{q}|\lambda_0 \approx 1$ for all three systems, where λ_0 is the wavelength of the observed CDW/PLD. This implies that the coherence lengths are as short as they can physically reasonably be, which again suggests that the short-coherence-length (strong-coupling) limit applies.

(v) It is not surprising that all three compounds can be regarded as quasi-2D ($2 < D < 3$), when comparing resistivity measurements parallel and perpendicular to the layers. However, the anisotropy ratio covers two orders of magnitude, $\rho_\parallel/\rho_\perp \approx 2.5$–500, which implies qualitative differences between the compounds. 1T-TaS$_2$ should be regarded as a 2D system, while 1T-TiSe$_2$ is almost 3D, and 2H-TaSe$_2$ is somewhere in between.

(vi) Finally, an interesting observation is that the maximum atomic displacement appears to scale linearly with the transition temperature: $u_{\max}/a \approx 1.27 \times 10^{-4} T_0$ (K), with T_0 referring to the transition between the normal phase and the first CDW/PLD phase reached upon cooling (an incommensurate CDW phase for 1T-TaS$_2$ and 2H-TaSe$_2$ and a commensurate CDW phase for 1T-TiSe$_2$). It is not clear whether this is accidental or implies a common underlying mechanism. However, if we combine the linear transition temperature dependences of the energy gap $\Delta(0)$ and of the maximum atomic displacement $u_{\max}$, we obtain a 'universal' electron–phonon coupling parameter $\Delta(0)/u_{\max} = (0.55 \pm 0.13)$ eV Å^{-1}.

Summing up, the key experimental observations—an electronic energy gap and a periodic lattice distortion at low temperatures as well as a Kohn anomaly at high temperatures—suggest a Peierls-like CDW/PLD instability in the three layer compounds 1T-TaS$_2$, 2H-TaSe$_2$ and 1T-TiSe$_2$. Yet, we foresee that the simple 1D weak-coupling mean-field theory will probably not describe the observed transitions adequately, because the materials are quasi-2D and in the intermediate to strong-coupling regime.

As pointed out in section 2.2, strong coupling implies that models based on special features of the Fermi surface alone will not work when trying to explain the microscopic origin of CDW/PLDs. Instead, a detailed look at the entire band structure is necessary. In addition, there is some uncertainty related to the sizes of the measured energy gaps, not only because different methods measure different gaps in the electronic spectrum, but also because it is not evident where exactly in **k** space the energy gap(s) should open up. In that respect, it is also not fully transparent what a spectroscopy such as ARPES is actually seeing in the CDW/PLD phases. For these reasons, it seems necessary to investigate in detail the band structures and spectral weight distributions of the three selected materials in their reconstructed phases.

4. Band structures and spectral weight distributions of reconstructed 1T-TaS$_2$, 2H-TaSe$_2$ and 1T-TiSe$_2$

In this section, our goal will be twofold: (i) to better understand the ARPES results obtained from 1T-TaS$_2$, 2H-TaSe$_2$ and

1T-TiSe$_2$ in the commensurate CDW/PLD phases and (ii) to find some clues to the possible CDW mechanism(s) in the electronic structure near the Fermi energy E_F. We will not perform (intransparent) density-functional theory calculations. Instead, our approach is to use an empirical tight-binding model that is as simple as possible but captures the essential aspects. We start with a brief review of the available ARPES results on the three selected compounds.

4.1. Review of ARPES results

In the last couple of years, numerous ARPES studies have been performed on 1T-TaS$_2$ [68, 77, 79, 92, 104–112], 2H-TaSe$_2$ [81, 82, 84, 85, 113, 114] and 1T-TiSe$_2$ [11, 86–89, 115, 116]. Here, we will concentrate on the CDW/PLD-induced changes to the single-particle energies and the accompanying redistribution of spectral weight. Possible many-body effects on the ARPES lineshapes will not be considered.

For each compound, we show in figure 6 characteristic electronic structure changes—as seen by ARPES—that occur near the Fermi level upon entering the commensurate CDW/PLD phase. The corresponding ARPES measurements were conducted at the Electronic Structure Factory endstation at beamline 7.0.1 of the Advanced Light Source in Berkeley, with an overall energy resolution of ~50 meV and with the samples heated and cooled to above and below the known CDW transition temperatures (sample temperatures and photon energies used are indicated in figure 6). From these ARPES results and the previous studies, we abstract the schematic view of the material-specific electronic structure changes shown in figure 7. In this figure the black lines reflect the respective band structures or Fermi surfaces in the normal and CDW phases, whereas the thick gray lines accentuate those electronic states that carry a large ARPES spectral weight in the CDW phases. We emphasize that our ARPES results (figure 6) are in good overall agreement with the most recently reported results [11, 85, 110]. Minor discrepancies are presumably due to matrix element effects connected with different experimental geometries and photon energies used.

Figure 7(a) reproduces the results of an early tight-binding calculation for 1T-TaS$_2$ [75], on which much of our current understanding of the band structure in the commensurate $\sqrt{13} \times \sqrt{13}$ CDW/PLD phase is based. In undistorted 1T-TaS$_2$, a single Ta 5d band disperses downwards from the Brillouin zone center (Γ point) toward the zone boundary (M point) and then back upwards along the zone face (M–K direction). It crosses the Fermi level twice to give an elliptical Fermi surface pocket centered on M (see figure 11(b)). In the $\sqrt{13} \times \sqrt{13}$ reconstructed phase, a dramatic rearrangement is predicted to occur. The occupied part of the Ta 5d band is split into submanifolds separated by gaps and the Fermi surface becomes 'messy', being determined by the bottom of a spaghetti-like set of bands (see figure 7(a) (right)).

The results of ARPES measurements on 1T-TaS$_2$ are in principle consistent with this picture. The existence of the submanifolds has been confirmed [75, 79, 104] and some of the fine structure within the submanifolds, including subband dispersions, has been resolved [77, 109–111]. This is illustrated in figure 7(a) by the thick gray lines. It should be pointed out, however, that relating ARPES data on 1T-TaS$_2$ to CDW effects is not unambiguous. First, there are no ARPES results available for the undistorted phase, which exists only in a small temperature interval above ~543 K (ARPES data for the highest sample temperature so far are shown in figure 6(a)). Yet, this is not too problematic. Since spectral weight distributions reflect the original band dispersion as long as the superlattice crystal potential is small (see section 2.1),

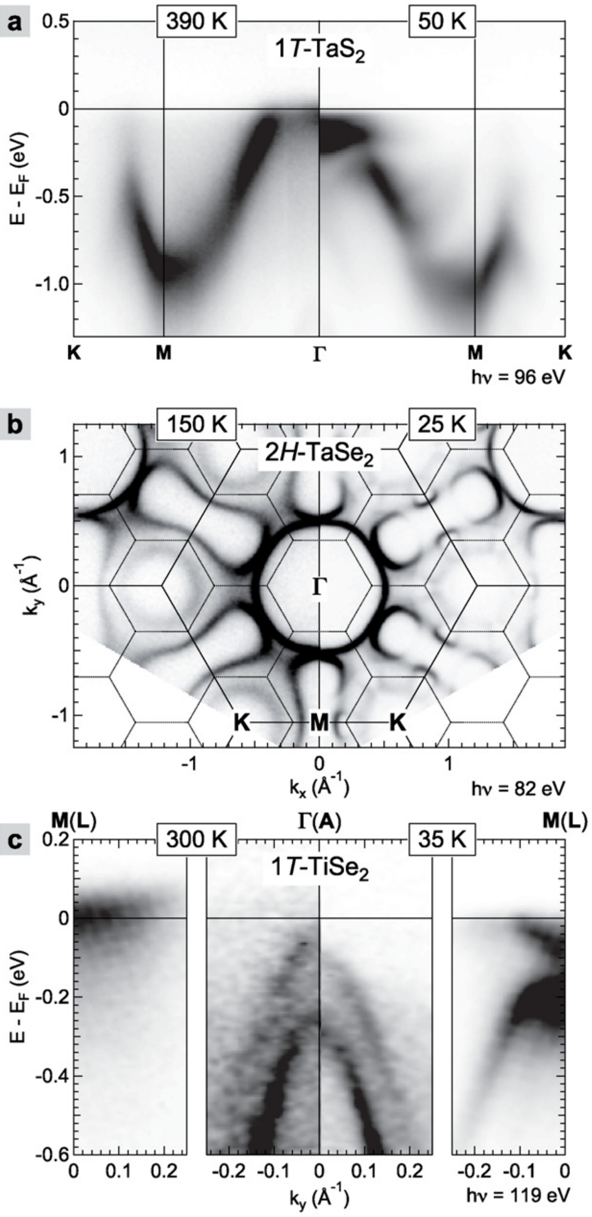

Figure 6. Experimental electronic structures of (a) 1T-TaS$_2$, (b) 2H-TaSe$_2$ and (c) 1T-TiSe$_2$, as seen by ARPES in the normal phases (left) and in the commensurate CDW phases (right). The corresponding temperature and photon energies are indicated. ARPES intensity maps are shown in inverse grayscale (black corresponding to high intensity). In (b) the Brillouin zones for the 1 × 1 (solid lines) and 3 × 3 (dotted lines) superlattices of 2H-TaSe$_2$ are indicated.

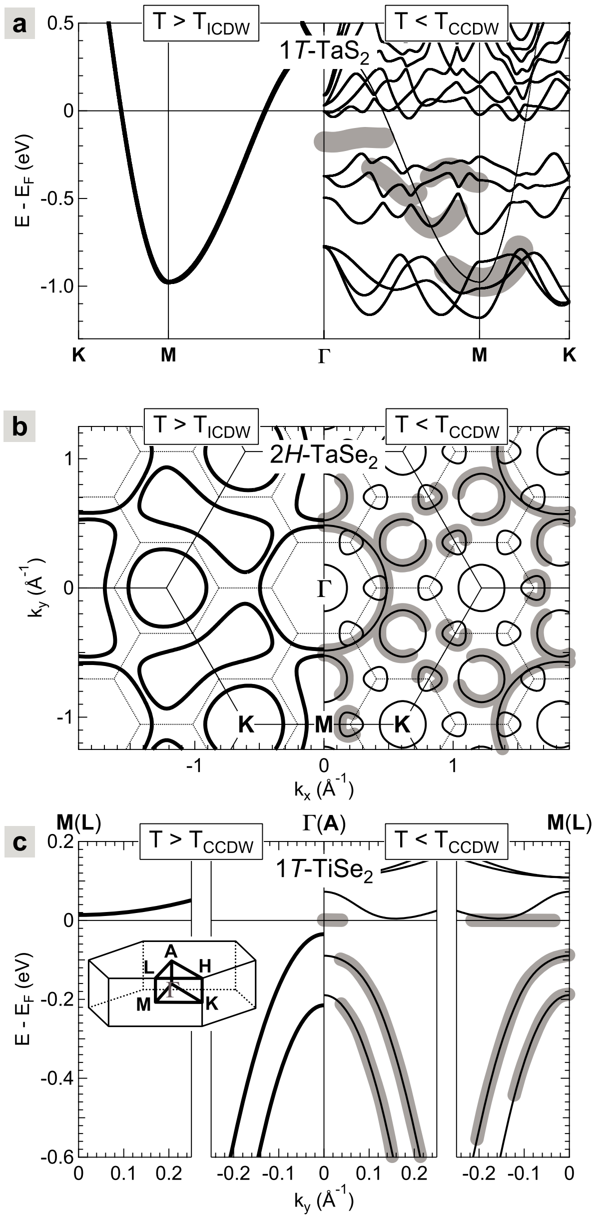

Figure 7. Schematic electronic structures of (a) 1T-TaS$_2$, (b) 2H-TaSe$_2$ and (c) 1T-TiSe$_2$, taken from experimental and theoretical band structure results in the normal phases (left) and in the commensurate CDW phases (right). Band structure features that carry significant spectral weight in the CDW phases are highlighted by thick gray lines. The inset in (c) shows the bulk Brillouin zone of the layered compounds.

the undistorted band dispersion can practically be extracted from room temperature ARPES data, when the system is in the nearly commensurate CDW phase. In fact, even deep in the commensurate CDW phase, the spectral weight is mostly concentrated along the original band and the reconstructed band structure is only faintly visible [109–111] (see also figure 6(a)). Second, the transition to the commensurate phase is accompanied by a Mott–Hubbard-type metal–insulator transition, which creates a ∼0.4 eV gap at E_F and leads to the appearance of a rather sharp Hubbard subband around Γ at ∼0.2 eV below E_F [68, 104, 110] (thick gray line in figure 7(a)). Hence, strong electron–phonon coupling and electronic correlations are simultaneously present in 1T-TaS$_2$ and this, together with the 'band spaghetti', leads to broad ARPES lineshapes and the absence of sharp Fermi level crossings [105, 106, 110, 111] (figure 6(a)). The experimental Fermi surface maps are diffuse; if unnormalized, they show a high-intensity feature centered on Γ and almost no intensity near the zone boundaries [108, 111]. The conclusion then is that there is considerable uncertainty in the band diagram depicted in figure 7(a) and in its relation to the measured spectral weight distributions. ARPES cannot resolve all the predicted fine details and the tight-binding model itself may not be fully appropriate, not least because it neglects the spin–orbit interaction, which is expected to be important in the valence band structure of Ta compounds.

For 2H-TaSe$_2$, the situation is different. The most recent ARPES data are extremely sharp and, therefore, allow for a quantitative analysis by fitting the data to tight-binding formulae [84, 85, 113, 114]. Here, we concentrate on the CDW-induced changes to the Fermi surface. Figure 7(b) compares the Fermi surface topologies in the normal and commensurate CDW states, as determined with high accuracy in [85, 113, 114]. In the normal phase (above 122 K), the Fermi surface of 2H-TaSe$_2$ consists of two hole-like circular pockets around Γ and around K and one electron-like 'dogbone' centered on M. Note that this topology was not clear until recently [84] and that it implies the existence of two saddle points in the band structure along the Γ–K direction, one above and the other below E_F. As a precursor of the CDW (at a temperature of ∼180 K), ARPES finds small pseudogaps on the K pocket and possibly also on parts of the M dogbone [85]. Upon entering the incommensurate CDW phase (between 90 and 122 K) these pseudogaps become larger, until they finally evolve into real bandgaps in the commensurate 3 × 3 CDW phase (below 90 K) [85]. As a result, the K Fermi surface pocket is completely destroyed and the M dogbone is broken up at the zone face, while the Γ pocket remains fully intact [84, 85]. The reconstructed Fermi surface appears to consist of circular pockets centered on the Γ points of the new Brillouin zones and rounded triangles around the new K points (see figures 6(b) (right) and 7(b) (right)). The spectral weight, however, is concentrated on the normal-state Γ pocket and on those parts of the other normal-state Fermi surface sheets that contribute to the reconstructed Fermi surface pockets [85]. In short, ARPES presents a comparatively lucid picture of the CDW-induced changes to the Fermi surface of 2H-TaSe$_2$ and the results suggest that the selective, **k**-dependent energy gapping should be given closer scrutiny.

In the case of 1T-TiSe$_2$, the relevant electronic states are the Se 4p states forming the valence band maximum in the zone center (at the Γ point) and the Ti 3d states of the conduction band minimum at the edge of the 3D Brillouin zone (at the L point, see the inset in figure 7(c)). In the commensurate 2 × 2 × 2 CDW phase (below 202 K), the Γ and L symmetry points of the normal reciprocal lattice become equivalent Γ points of the smaller Brillouin zones so that the Se 4p and Ti 3d bands can interact directly, if they are close enough in energy. Although a consensus on the magnitude and sign of the p–d gap in the normal phase has not yet been reached, the most recent ARPES results have yielded sufficiently small gap values between -20 meV (band overlap) and $+150$ meV (bandgap) for the p–d interaction to play an important role in the band energy lowering in the CDW phase [11, 86, 87, 89, 116]. Figure 7(c) reproduces the quantitative ARPES results of [87]. (Note that there are only two Se 4p bands depicted at Γ, while there should be three. The third band has probably escaped detection because of the use of an inappropriate photon energy in the experiment.) Upon the transition from the normal state to the commensurate CDW state, 1T-TiSe$_2$ transforms from a semiconductor with a small indirect gap of $\sim$50 meV between Γ and L to another semiconductor with a larger indirect gap of $\sim$100 meV at a slightly different location in $\mathbf{k}$ space. In other ARPES studies, similar p-band shifts to lower energies are reported [11, 86, 87, 89] (see also figure 6(c)). Besides this opening of a p–d gap, the strong p–d band interaction manifests itself in the flattening of the top of the Se 4p valence bands, the suppression of spectral weight near the top of these bands, the buckling of the bottom of the Ti 3d conduction band and the appearance of remarkably intense folded Se 4p bands at L (see figures 6(c) and 7(c)). The further supposed splitting of the threefold-degenerate conduction band in the unoccupied region [87] is not observable by ARPES. Summing up, there is clear evidence from ARPES that p–d band interaction is an important ingredient for the CDW phase transition in 1T-TiSe$_2$. Thus, if the nature of the interaction could be further clarified, this would certainly contribute to a better understanding of the transition.

It should be pointed out that in all three compounds precursors to the effects observed in the commensurate CDW/PLD phases—such as a pseudogap, diffuse shadow band intensity or suppression of spectral weight—already occur well above the transition temperatures to these phases. In addition to the experimental signatures of the CDW/PLD states discussed in section 3.2, this is further evidence for the strong-coupling nature of the CDW/PLDs in these materials.

How do the ARPES results on the three selected layered CDW/PLD systems comply with the simple 1D weak-coupling mean-field picture described in section 2.1? Where do the CDW/PLD-induced energy gaps actually open up? As anticipated in sections 2.2 and 2.3, strong coupling and two-dimensionality blur the image of a Fermi surface-driven instability; the CDW gap in the electronic spectrum does not necessarily open up at E_F. It does so in 2H-TaSe$_2$, in which the K Fermi surface pocket is completely (and the M pocket partially) removed. But in 1T-TaS$_2$ and in 1T-TiSe$_2$ the CDW gaps are not directly connected with Fermi level crossings of the undistorted bands. Instead, gaps open up between subband manifolds at somewhat higher binding energies. The CDW gapping occurs in 1T-TaS$_2$between subgroups of occupied Ta 5d bands and in 1T-TiSe$_2$ between the bottom of the (nominally unoccupied) Ti 3d conduction band and the top of the (fully occupied) Se 4p valence band.

To what extent is the novel periodicity of the CDW/PLD phase reflected in the band dispersions? We have noted above that reconstructed or 'shadow' bands carry significant spectral weight only in the proximity of original bands so that spectroscopy cannot detect the whole folded-out band structure, except for faint shadows in the regions away from the original bands. Although this picture is in principle confirmed by the ARPES results on the layered compounds, the relative strength and clarity of the shadow band effects is surprising. In 1T-TaS$_2$, the compound with the largest lattice distortion, the fine structure in the reconstructed band structure is only faintly visible, while in 2H-TaSe$_2$ and even more so in 1T-TiSe$_2$ clear signatures of isolated reconstructed bands can be identified—in 2H-TaSe$_2$ in the Fermi surface map and in 1T-TiSe$_2$ in the band map around the L point.

Our goal will now be to understand these band structure effects on the basis of an empirical tight-binding model. An important motivation is the following: if the model can reproduce the experimentally observed spectral weight distributions, it may provide access to the complete reconstructed band structure and not just the parts with a high spectral weight that are detectable by ARPES. Based on such a foundation, the discussion of the possible CDW mechanisms is expected to become richer.

4.2. Empirical tight-binding model

Our approach to simulating the electronic structure effects upon CDW/PLD formation is based on the simplest model that incorporates the essential physics, namely the Slater–Koster tight-binding model. The tight-binding scheme we use follows the one outlined in [75, 117–119].

The first step is a fit of the Slater–Koster parameters, using a minimal basis set, to a first-principles band structure calculation [93, 117, 120]. For 1T-TaS$_2$ and 2H-TaSe$_2$, we use only Ta 5d orbitals, and for 1T-TiSe$_2$ the basis consists of the three Ti 3d t$_{2g}$ and the six Se 4p orbitals. In the case of 1T-TaS$_2$, the Hamiltonian includes only nearest-neighbor intralayer d–d interactions, but for 2H-TaSe$_2$ these are augmented by nearest-neighbor and second-neighbor d–d interlayer interactions. For 1T-TiSe$_2$, on the other hand, only nearest-neighbor p–p, p–d and d–d intralayer and interlayer interactions are considered. In the case of the two Ta compounds, spin–orbit coupling is added by inclusion of the intra-atomic matrices M and N of Abate and Asdente [121] and by use of the Herman–Skillman value of the spin–orbit parameter ($\xi = 0.313$ eV) [122]. In this way, we end up with reduced Hamiltonians of dimension 10 (1T-TaS$_2$), 20 (2H-TaSe$_2$) and 9 (1T-TiSe$_2$). The fitted tight-binding band structures are shown in figures 8(a), 9(a) and 10(a). For the two 'three-dimensional' compounds 2H-TaSe$_2$ and 1T-TiSe$_2$, we restrict our analysis to the ALH and ΓMK planes in reciprocal space, respectively.

The second step in our scheme is the simulation of the effects of the reconstruction. This is done as previously described [75, 118, 119]. The Hamiltonians of the unreconstructed phases are opened out into the larger unit cells depicted in figure 4, giving new Hamiltonians with dimension 130 (1T-TaS$_2$), 180 (2H-TaSe$_2$) and 36 (1T-TiSe$_2$). To simulate the reconstruction, the Slater–Koster hopping d–d, p–d and p–p integrals are scaled as r^{-5}, r^{-4} and r^{-3}, respectively, where r is the interatomic distance [123]. Some bonds within the distortion patterns are thereby strengthened and other bonds

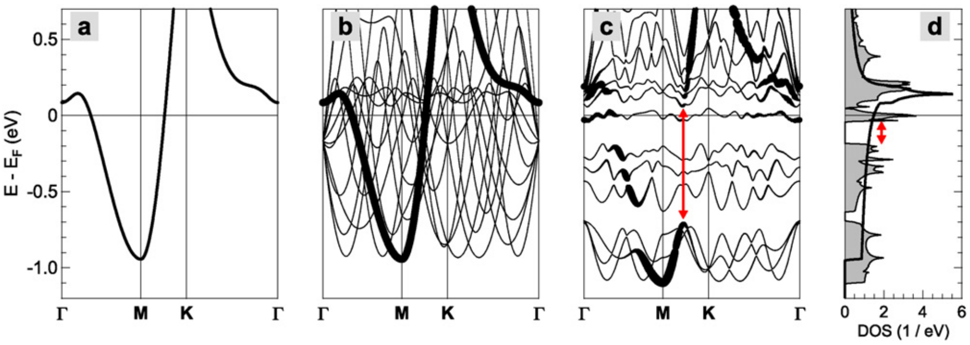

Figure 8. Evolution of the band structure of 1T-TaS$_2$ from the unreconstructed to the $\sqrt{13} \times \sqrt{13}$ reconstructed phase. (a) Unreconstructed band structure. (b) Unreconstructed band structure plus umklapp bands generated by translation through the reciprocal lattice vectors of the reconstructed Brillouin zone. (c) Reconstructed band structure with inclusion of the bond strengthenings within the distortion pattern (for the observed Ta atom displacement of $0.07a$). In (c) and (d) the symbol size is proportional to the spectral weight carried by the states.
(d) Density of states in the unreconstructed (thick solid line) and reconstructed (filled gray curve) case. The red arrows mark pronounced gaps in the spectral weight distribution and density-of-states curve.

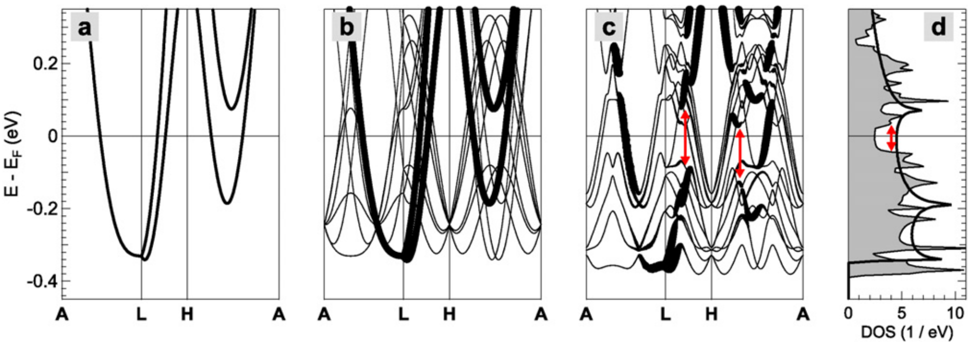

Figure 9. Evolution of the band structure of 2H-TaSe$_2$ from the unreconstructed to the 3 × 3 reconstructed phase. (a) Unreconstructed band structure. (b) Unreconstructed band structure plus umklapp bands generated by translation through the reciprocal lattice vectors of the reconstructed Brillouin zone. (c) Reconstructed band structure with inclusion of the bond strengthenings within the distortion pattern (for the observed Ta atom displacement of $0.015a$). In (c) and (d) the symbol size is proportional to the spectral weight carried by the states.
(d) Density of states in the unreconstructed (thick solid line) and reconstructed (filled gray curve) case. The red arrows mark pronounced gaps in the spectral weight distribution and density-of-states curve.

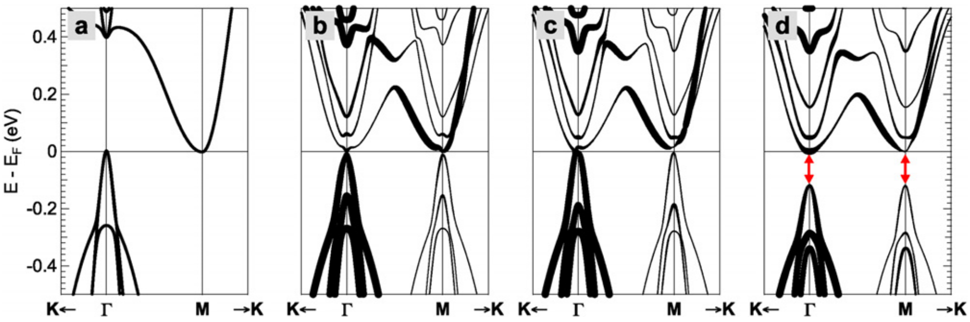

Figure 10. Evolution of the band structure of 1T-TiSe$_2$ from the unreconstructed to the 2 × 2 reconstructed phase. (a) Unreconstructed band structure. ((b)–(d)) Reconstructed band structure with inclusion of the bond strengthenings within the lattice distortion pattern: (b) zero distortion amplitude, (c) the observed distortion amplitude (corresponding to a Ti atom displacement of $0.024a$) and (d) twice the observed distortion amplitude. In (b)–(d) the symbol size is proportional to the spectral weight carried by the states. The red arrows highlight the opening of the Se 4p–Ti 3d bandgap.

are weakened. Since the bond-length changes are known from experiment, there remain no further disposable parameters in the model. To keep the analysis as simple as possible, we ignore any slight non-radial atomic movements [62] in the formation of the lattice distortion patterns and, for 1T-TiSe$_2$, we neglect the reconstruction in the z direction.

The third step is to calculate the distribution of spectral weight over the reconstructed band structure. To this end, we

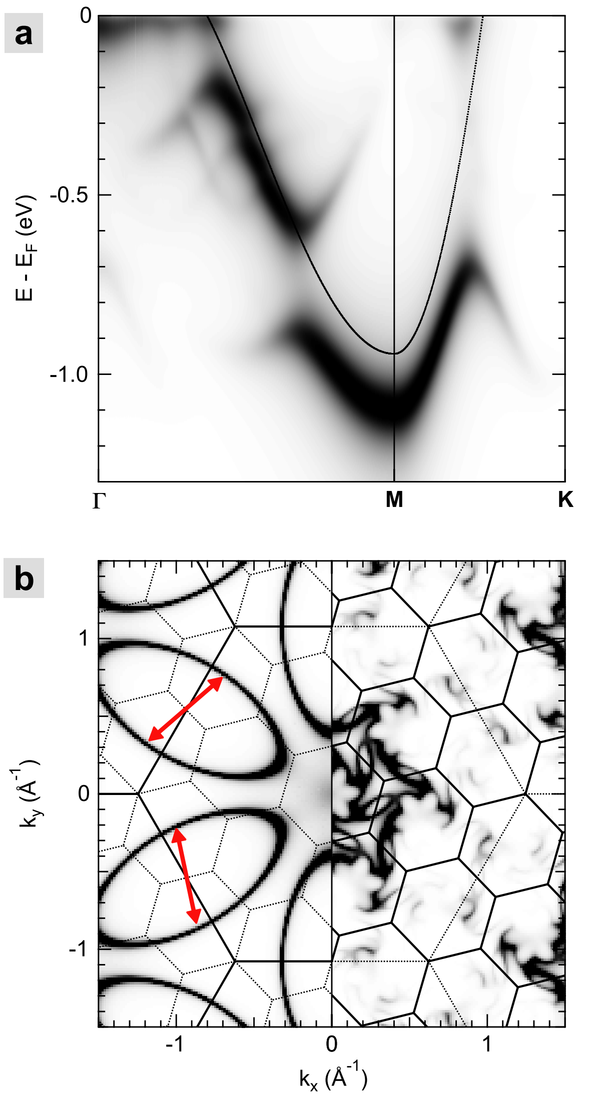

Figure 11. Simulated spectral weight distributions of 1T-TaS$_2$ (a) Band map along Γ–M–K in the commensurate $\sqrt{13} \times \sqrt{13}$ CDW state. The solid line refers to the undistorted band dispersion. (b) Fermi surface map in the normal state (left) and in the commensurate $\sqrt{13} \times \sqrt{13}$ CDW state (right). The Brillouin zones of the normal and reconstructed phases are indicated. The red arrows mark possible nesting vectors.

have extended the 'spectral function' approach for the simple two-band case, as described in section 2.1, to the case with multiple reconstructed bands (see also [79, 124, 125]). If we denote the original 'main' bands by $E_\lambda(\mathbf{k})$, the reconstructed bands by $E'_j(\mathbf{k})$ and the corresponding eigenstates by $|\lambda\mathbf{k}\rangle$ and $|j\mathbf{k}\rangle$ (with band indices λ and j), the total spectral weight carried by the reconstructed eigenstate $|j\mathbf{k}\rangle$ (having energy $E'_j(\mathbf{k})$) is given by $\sum_\lambda |\langle j\mathbf{k}|\lambda\mathbf{k}\rangle|^2$, i.e. by the projection of the reconstructed eigenvector onto the original eigenvectors. Thus, the spectral weight distribution function, depending on wavevector $\mathbf{k}$ and energy ω, becomes

$$A(\mathbf{k}, \omega) = \sum_{\lambda, j} |\langle j\mathbf{k}|\lambda\mathbf{k}\rangle|^2 \delta(\omega - E'_j(\mathbf{k})). \qquad (28)$$

Figures 8, 9 and 10 illustrate our tight-binding approach by showing the progressive effects of the CDW/PLD reconstruction on the band structures of 1T-TaS$_2$, 2H-TaSe$_2$ and 1T-TiSe$_2$ near the Fermi level. First, the original bands (figures 8(a), 9(a) and 10(a)) are opened out into the larger unit cells creating a 'spaghetti' of umklapp bands (figures 8(b), 9(b) and 10(b)). These 'shadow' bands are simply obtained by translation through the reciprocal lattice vectors of the smaller Brillouin zones (see figure 4). Then, the bond strengthenings and weakenings are introduced (figures 8(c), 9(c) and 10(c)), which leads to considerable changes: band degeneracies are lifted, bands are shifted, energy gaps are created and spectral weight is redistributed. Let us now discuss these effects for each compound in more detail.

4.3. Tight-binding results

$\sqrt{13} \times \sqrt{13}$ modulation in 1T-TaS$_2$. In 1T-TaS$_2$, the PLD amplitude is the largest and therefore the band structure changes are the most pronounced (the maximum Ta atom displacement is $\sim 0.07a$). The reconstructed band structure collapses into submanifolds separated by distinct energy gaps [75, 118] (see figures 8(c) and 8(d)). There are two low-lying three-band submanifolds, each containing six electrons. The 'thirteenth' electron (there are 13 Ta 5d^1 atoms in the reconstructed unit cell) resides in a distinct band at the Fermi level. Since this band has a small width ($\sim$80 meV), it is susceptible to a Mott–Hubbard transition, as proposed originally by Fazekas and Tosatti [67] and later confirmed by ARPES [68]. We have shown previously that reconstruction and spin–orbit interaction are both essential for the isolated band to occur [118]. This band represents the important difference compared to the earlier tight-binding results [75] plotted in figure 7(a). The new results suggest that the Mott–Hubbard-type transition which is connected with the nearly commensurate-CDW–commensurate-CDW transition in 1T-TaS$_2$ appears as a consequence of the favorable electronic structure of the commensurate-CDW phase. Since the observed Mott–Hubbard gap is relatively small [68], its contribution to the stabilization of the commensurate-CDW phase is presumably negligible.

As expected, the calculated spectral weight is concentrated along the original main band (figure 8(c)). To facilitate a better comparison with ARPES results, we show simulated spectral weight distributions in figure 11. These are obtained by replacing the delta function in equation (28) with a Lorentzian of 100 meV full width at half-maximum. Both the $A(\mathbf{k}_\parallel, E)$ band map along Γ–M–K (figure 11(a)) as well as the $A(\mathbf{k}_\parallel, E_\mathrm{F})$ Fermi surface map (figure 11(b)) are in good qualitative agreement with the results of ARPES measurements (see [108–111]). Unfortunately, ARPES cannot resolve the predicted fine details because of lifetime and resolution effects, although recently shadow band dispersions exhibiting the CDW periodicity have been detected [110, 111]. Two features reproduced by the simulation are remarkable: the large spectral weight gap along the M–K direction (figures 8(c) and 11(a)) and the related strong spectral weight suppression in the Fermi surface map near the Brillouin zone boundary (figure 11(b)). The tight-binding simulation shows that both effects are natural

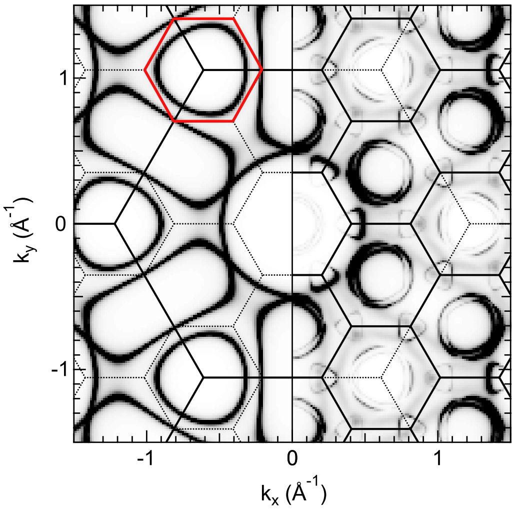

Figure 12. Simulated Fermi surface maps of 2H-TaSe$_2$ in the normal state (left) and in the commensurate 3 × 3 CDW state (right). The Brillouin zones of the normal and reconstructed states are indicated. The small Brillouin zone highlighted in red emphasizes the near match with the normal-state Fermi surface pocket centered on the K(H) point.

consequences of the lattice distortion in the CDW phase; electron localization or photoemission matrix element effects are not required for their explanation [107].

It should be pointed out that the large spectral weight gap along M–K is not the CDW gap, although it occurs in a region of **k** space where large parallel parts of the elliptical Fermi contours are spanned by the observed CDW wavevector and therefore significant Fermi surface nesting may be expected (see red arrows in figure 11(b)). The 'true CDW gaps' are rather the gaps between the subband manifolds. We emphasize that it is the energy lowering of the two low-lying three-band submanifolds that stabilizes the commensurate CDW/PLD, and not the lowering of states at E_F. In fact, in the tight-binding calculation the density of states at E_F even increases in the CDW phase, due to the emergence of the distinct and narrow band straddling the Fermi level (figure 8(d)). By summing over all occupied states, we find a relatively large total electronic energy gain of 160 meV per Ta atom for the experimentally observed PLD amplitude.

3 × 3 *modulation in 2H-TaSe*$_2$. In 2H-TaSe$_2$, the maximum displacement of the Ta atoms in the CDW phase (∼0.015a) is about a factor of five smaller than in 1T-TaS$_2$. Consequently, the electronic structure changes are less dramatic. The reconstructed band structure does not collapse into submanifolds (figure 9) and the reconstructed Fermi surface (in the repeated zone scheme) retains much more resemblance to the original Fermi surface (figure 12). Nevertheless, the PLD-induced changes are significant. The Fermi surface pocket around K(H) is destroyed (red arrows in figure 9(c)), the M(L) dogbone is broken up (figure 12) and the new Fermi surface consists of (doubly degenerate) pockets centered on the new Γ(A) points and of small rounded triangles around the new K(H) points (figure 12). Note that the calculated spectral weight distribution at E_F shown in figure 12 agrees remarkably well with the ARPES results (figures 6(b) and 7(b)).

It is tempting to associate the occurrence of the 3 × 3 CDW/PLD in 2H-TaSe$_2$ with the near coincidence of the K(H) Fermi surface pocket with the edges of the new Brillouin zone (see the red hexagon in figure 12). This scenario would be in direct analogy with the Peierls instability in one dimension, where, however, the coincidence between Fermi surface and new Bragg planes is exact (see section 2.1). Since gaps are created in the band structure near the new Bragg planes, the K(H) pocket will readily disappear when the 3 × 3 PLD sets in. The opening of the pseudogap in the density of states near E_F (marked by a red arrow in figure 9(d)) is the consequence. Yet, one cannot claim that the CDW/PLD instability is purely Fermi-surface-driven, because the occupied states well below E_F contribute significantly to the total electronic energy gain (see figure 9(d)). For the experimentally observed PLD amplitude, the calculated band structure energy lowering is 20 meV per Ta atom, in good agreement with the value of 26 meV per Ta atom reported in [126].

2 × 2 *modulation in 1T-TiSe*$_2$. In 1T-TiSe$_2$, the maximum displacement of the transition metal is ∼0.024a, about 1.5 times larger than in 2H-TaSe$_2$ and about a factor of three smaller than in 1T-TaS$_2$. The relevant electron states (of Se 4p and Ti 3d character) are confined to small volumes in **k** space in the center and on the face of the Brillouin zone. The CDW superlattice unit cell is the smallest for the three compounds so that the number of umklapp bands is the lowest. Nevertheless, the band structure changes due to the PLD are not less intricate.

For undistorted 1T-TiSe$_2$, we assume the band line up depicted in figure 10(a). There are three hole-like Se 4p bands around Γ—two degenerate Se 4p$_{x,y}$ bands comprising the valence band maximum and one Se 4p$_z$ band at lower energy—and one electron-like Ti 3d band around M(L). Note that spin–orbit coupling and band dispersion in the layer-perpendicular direction are neglected in the calculation. The indirect Se 4p–Ti 3d bandgap is set to zero, as a compromise between the latest ARPES results [11, 86–89, 115, 116]. In the folded-out band structure, the Ti 3d band becomes threefold-degenerate, as there are three independent M(L) points in the first Brillouin zone. Remarkably, this degeneracy and also the Se 4p$_{x,y}$ degeneracy at Γ are lifted in the reconstructed band structure already for zero distortion amplitude (figure 10(b)). There are now three separate Se 4p bands and three separate Ti 3d bands at the equivalent Γ and M(L) points, but the p–d gap remains zero. It even stays zero when the PLD amplitude is increased to the experimentally observed value (figure 10(b)), the major effect being that the relative band edge positions within the Se 4p and Ti 3d manifolds are changed. For twice the observed distortion amplitude, however, a p–d gap of ∼100 meV opens up, as indicated by the red arrows in figure 10(d). This gap value is in good agreement with ARPES measurements (figure 7(c)).

Upon increasing the maximum Ti atom displacement from zero to 0.048a, spectral weight is continuously transferred from the Se 4p to the Ti 3d states at Γ and vice versa at M(L) (figures 10(b)–(d)). For better comparison with ARPES

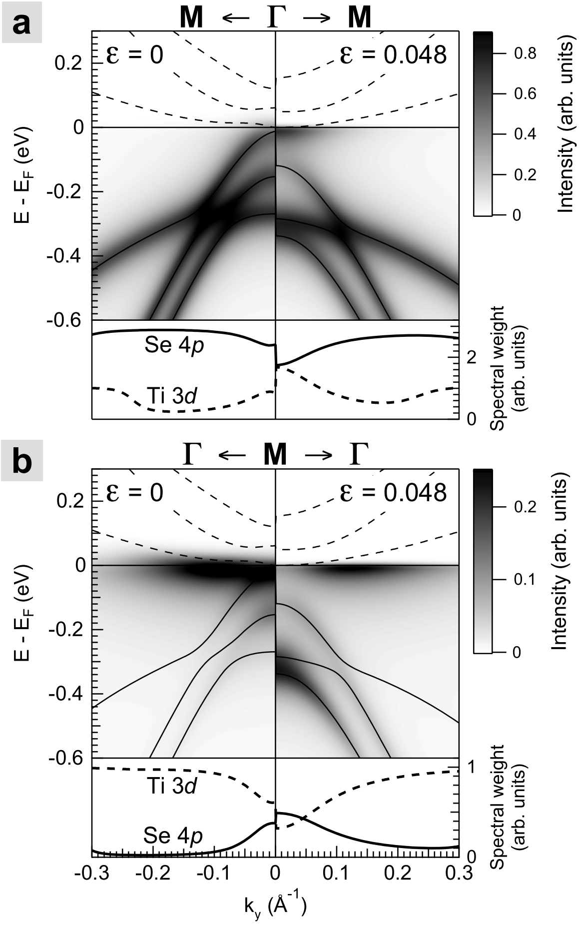

Figure 13. Simulated spectral weight distributions of 1T-TiSe$_2$ for the commensurate 2×2 CDW state: (a) around the Γ point and (b) around the M(L) point. On the left, the Ti atom displacement relative to the in-plane lattice parameter is zero; on the right, it is 4.8% (i.e. twice the experimentally observed value). The spectral weight functions are multiplied by a Fermi–Dirac cutoff. Se 4p bands are denoted by solid lines and Ti 3d bands by dashed lines. In the bottom panels, the total spectral weight carried by each band manifold is shown.

results, figure 13 shows calculated spectral weight distributions for the interesting regions around the Γ and the M(L) point. The qualitative agreement between the measured and simulated band maps is good (see figure 7(c)). Among the key features that are reproduced by the tight-binding model are—near Γ (figure 13(a))—the flattening of the Se 4p valence bands, the loss of spectral weight near the valence band maximum, the appearance of Ti 3d spectral weight near E_F and—near M(L) (figure 13(b))—the occurrence of intense folded valence bands and an E_F intensity maximum away from the symmetry point [11]. A striking result is the strong spectral weight transfer at the high-symmetry points (see the bottom panels of figures 13(a) and (b)). For a Ti atom distortion only twice as large as the observed one, the total spectral weight carried by the shadow bands at Γ and at M(L) is larger than that of the original bands. This is in contrast to [11], where it has been argued that the atomic displacements in the CDW phase of 1T-TiSe$_2$ are far too small to produce significant spectral weight transfer to the shadow bands.

What are the implications of these results on the CDW mechanism in 1T-TiSe$_2$? In principle, the tight-binding model confirms the scenario proposed in [87] (figure 7(c)). The PLD causes a splitting of the degenerate Ti 3d conduction band and Ti 3d–Se 4p band repulsion leads to a lowering of the top of the valence band and thereby of the total band energy. A novel feature revealed in the present study is the PLD-induced splitting of the top two Se 4p bands. Note that in ARPES studies this splitting has commonly been attributed to spin–orbit interaction alone [127]. Since CDW fluctuations are known to affect the normal-phase band structure of 1T-TiSe$_2$ as seen by ARPES, it seems not unreasonable that there is a significant CDW-induced contribution to the observed p-band splitting even at room temperature.

As to the origin of the CDW/PLD in 1T-TiSe$_2$, two issues are the most pressing. First, as the **k**-space volume involved in the transition appears to be small, one may ask whether the observed changes in the electron energies near E_F are sufficient to drive the transition. By summing over all occupied states in the energy range from -0.6 eV to $E_F = 0$, we obtain a band energy gain of ~20 meV per Ti atom. This value agrees fairly well with the 27 meV per Ti atom reported in [23] and it is comparable to the value obtained for 2H-TaSe$_2$, the compound with somewhat similar PLD amplitude and transition temperature. So, stabilization of the CDW/PLD by the one-electron total energy change appears to be possible. The second question is whether the PLD is solely responsible for the observed changes (‘pure’ Peierls instability) or whether there is a significant excitonic contribution (combined Peierls–excitonic insulator instability [128–130]). Our tight-binding results suggest the latter. The most significant ARPES result for reconstructed 1T-TiSe$_2$ is the opening of the relatively large p–d gap and this is not reproduced by the present model until the Ti atom displacement reaches twice the experimentally observed value.

To sum up, the magnitude, **k** dependence and origin of the CDW gap in the layered transition-metal dichalcogenides were at the focus of many ARPES studies in the past. For the three selected compounds 1T-TaS$_2$, 2H-TaSe$_2$ and 1T-TiSe$_2$, quantitative results, when available, have been summarized in figure 7. We find it remarkable that the key features of these results can be reproduced by empirical tight-binding calculations. Considering the simplicity of the model, the similarity between simulated spectral weight distributions and measured ARPES intensity maps is striking. The tight-binding results corroborate that CDW gapping in the three compounds is large, not restricted to a small interval around the Fermi energy and strongly **k**-dependent. There is not one uniform gap opening up at the Fermi energy; rather subbands are shifted over extended parts of the Brillouin zone. The results also demonstrate that the observed band structure changes lower the total energy of the electron system significantly and that they are a natural consequence of the observed atomic distortion patterns. The concept of Fermi surface nesting was not relevant in the analysis, although some connection between the band structure near the Fermi level and the observed CDW/PLD wavevectors can be drawn for all three compounds.

5. Why do CDW/PLDs occur in the layer compounds?

One can try to understand the occurrence of CDW/PLDs in the layered transition-metal dichalcogenides, in general, on different levels of sophistication. In the simplest approach, the observed CDW/PLD wavevectors may be rationalized from the **k**-space geometry of the electronic structure in a narrow energy window around E_F or the CDW/PLD formation may be qualitatively explained by analyzing the observed lattice distortion patterns. On a higher level, the question of whether a CDW/PLD should occur at all may be answered by considering the balance between band structure energy gain and elastic energy cost within simplified zero-temperature models. But finally, for a prediction of the CDW/PLD transition temperatures, a full microscopic theory at finite temperatures is necessary. Here, we will proceed along this line, from the simple to the more sophisticated explanations.

We emphasize that there need not be one underlying CDW mechanism for the compounds we have concentrated on; the formation of the different CDW/PLD superstructures may easily be caused by different driving forces, particularly because the electronic structures and resulting transport properties of the three selected materials are so different. Yet, a unifying explanation would be nice and, eventually, all three CDW systems belong to the same family of compounds and electron–phonon coupling is strong in all of them. As has been pointed out previously [131, 132], the general occurrence of CDW/PLDs in these materials makes it seem reasonable that the phenomenon is based on general features rather than specific and subtle properties of the band structure.

Our working hypothesis will thus be that the physical picture provided by the Peierls model, as detailed in section 2, is in principle correct for 1T-TaS$_2$, 2H-TaSe$_2$ and 1T-TiSe$_2$ and that the occurrence of the CDW/PLDs can be understood on the basis of a few measured and calculated parameters, such as T_0, $\mathbf{q}_0$, u_0, $\chi_0(\mathbf{q}_0)$ and $2g^2_{\mathbf{q}_0}/\hbar\omega_{\mathbf{q}_0}$. Naturally, this semi-quantitative approach is still overly simplistic, but it may be instructive anyway, given that the involved concepts and arguments are so commonly applied. It is an approach reflecting an experimentalist's view and the hope is that a hierarchy of factors determining CDW/PLD formation in the layered compounds can be established.

5.1. Qualitative explanations

Qualitative explanations of CDW/PLD formation are typically based on two extreme limits of the same physical phenomenon [38, 39] (see section 2.2). When the CDW/PLD amplitude is small, a metallic bonding picture applies; the coherence length is long, the energy gap small, the CDW/PLD often incommensurate and the transition is driven by an instability of the Fermi surface. At the other extreme, when the CDW/PLD amplitude is large, an ionic–covalent bonding picture is more appropriate; the coherence length is short, the energy gap large, the CDW/PLD tends to be commensurate and the driving force of the transition is a tendency to form shortened bonds between neighboring atoms such that the sum of the energies of shortened and lengthened bonds is lower than the energies of the normal bonds. The tight-binding results presented in the previous section can essentially be understood in the spirit of such a local-chemical-bonding picture.

1T-TaS$_2$ is an example for how one passes from one extreme to the other by lowering the temperature. For the incommensurate CDW/PLD in the hole-doped compound 1T-Ta$_{1-x}$Ti$_x$S$_2$ ($0 \leqslant x \leqslant 1$), electron diffraction has revealed a direct relationship between the size of the Fermi surface and the CDW/PLD wavevector $\mathbf{q}_0$, $|\mathbf{q}_0| \propto \sqrt{1-x}$ [56]. As such a correlation is expected for a nesting vector across the M centered elliptical Fermi surface pocket (see figure 11) shrinking as a function of hole doping x, the experimental finding strongly supports the idea of Fermi surface nesting as the driving force of the normal-to-incommensurate CDW/PLD phase transition. On the other hand, x-ray photoelectron spectroscopy [133] and scanning tunneling microscopy [134] measurements as well as model calculations [75] suggest that 1T-TaS$_2$ in the commensurate phase can be regarded as a mixed valence compound since there are inequivalent Ta sites differing by up to $0.4e^-$ per atom. This indicates a dominant role of the local bonding properties in the transition. In terms of local bonding energies, the transition is understood as follows: 13 Ta atoms form a star-shaped cluster (figure 4) in such a way that the occupied Ta 5d t$_{2g}$ levels split into three submanifolds with collectively lower energy [24, 67, 75, 118] (figure 8).

For 2H-TaSe$_2$, similar explanations can be given. ARPES measurements [84, 85, 113] suggest that the observed CDW/PLD wavevector is consistent with partial nesting of the K(H) Fermi surface pocket with the M(L) dogbone and with the Γ(A) pocket (see figure 12). Moreover, figure 12 illustrates that the Fermi surface around the K(H) point is very near to the faces of the novel Brillouin zone produced by the PLD. This is in close analogy to the archetypal 1D scenario of perfect nesting, in which a Peierls instability is bound to occur (see figure 1). Since Brillouin zone faces are planes of energy discontinuity, one expects large energy gapping on the K(H) pocket and this is indeed what is observed [84, 85]. On the other hand, the occurrence of the 3 × 3 CDW/PLD may also be explained by looking at the lattice distortion pattern in the Ta plane [24] (figure 4). There, nine-atom clusters are formed, leading in the electronic structure to a splitting of the Ta 5d$_{x^2-y^2,xy}$ manifold into two submanifolds. The lower one is associated with shortened and the upper one with lengthened metal–metal bonds. Since the Fermi level falls in the (pseudo-)gap between the two corresponding density-of-states peaks (see figure 9), the distorted structure is energetically more favorable.

In 1T-TiSe$_2$, the situation is different. The Se 4p and Ti 3d Fermi surface pockets (if they exist at all) are small and exhibit different sizes and anisotropies so that Fermi surface nesting can be ruled out. Nevertheless, the band structure topology is suggestive of the observed CDW/PLD wavevector, since $\mathbf{q}_0$ connects the Se 4p valence band maximum at Γ with the Ti 3d conduction band minimum at L. The resulting direct p–d interaction is a key element in the CDW/PLD transition. Because the band edges are close in energy, p–d hybridization occurs and the occupied p states are pushed to lower energies, thereby stabilizing the

CDW/PLD state. The often discussed question is whether the p–d interaction is phononic [23, 24, 47, 135, 136] or electronic (excitonic) [11, 137–140] in origin. When the coupling occurs via phonons, the transition is seen as a (Peierls-like) Jahn–Teller band instability and the one-electron total energy change connected with the PLD is the driving force. In terms of chemical bonding, the Se 4p band energy lowering can then be linked to the Ti–Se bond shortening in the observed distortion pattern [24] (figure 4). If, on the other hand, the p holes and d electrons are coupled via direct Coulomb interaction, one has the excitonic insulator scenario described in section 2.4 and the exchange–correlation energy change associated with the CDW is an important factor. The instability is then primarily electronic, even though it will be accompanied by a PLD due to finite electron–phonon coupling. Both models can qualitatively explain the CDW/PLD phase transition in 1T-TiSe$_2$. In view of the strong electron–phonon coupling in this material, however, the Jahn–Teller band instability seems more natural, although our tight-binding calculations have indicated that the experimentally observed lattice distortion amplitude is not sufficient to produce the p–d gap seen by ARPES. This leaves room for a significant excitonic contribution [128–130].

In summary, the ideas presented here may have some merit in qualitatively explaining why the observed CDW/PLD phases may occur in the three selected compounds. It is clear, however, that their success originates in knowing beforehand what is going to be explained. The concepts of Fermi surface nesting and local chemical bonding have very limited predictive power regarding the CDW/PLD wavevectors and they definitely cannot predict whether the CDW/PLD phase transitions should occur at all. Also, in a general situation, it does not seem reasonable to separate Fermi surface and local bond contributions [131] or, with regard to 1T-TiSe$_2$, one-electron and exchange–correlation energy contributions [38]. Consequently, we now move on to less specific, more quantitative microscopic models.

5.2. Existence of a CDW/PLD at $T = 0$

If a CDW/PLD is to occur at all, there must be a total energy gain resulting from distorting the lattice at $T = 0$: The electronic energy gain $\delta E_{\mathrm{electrons}} < 0$ arising from the band structure and exchange–correlation energy change has to overcome the lattice energy cost $\delta E_{\mathrm{lattice}} > 0$, i.e. $\delta E_{\mathrm{total}} = \delta E_{\mathrm{electrons}} + \delta E_{\mathrm{lattice}} < 0$. Whether the energy balance is indeed negative can, for example, be tested by using the Chan–Heine criterion, equation (9), or by comparing the calculated one-electron band energy change with a phenomenological lattice energy term. Here we will do both. The first approach has the advantage that it includes all relevant factors; but the electronic energy change is derived from perturbation theory and **k** dependence is neglected. In the second approach, on the other hand, the band structure energy change is more realistic; but the effects of electron–electron interactions are neglected.

In order to check the Chan–Heine condition (9), we have to estimate the involved microscopic quantities for the three selected materials: 1T-TaS$_2$, 2H-TaSe$_2$ and 1T-TiSe$_2$. The results, from this work and compiled from the literature, are summarized in table 5. The values for the electronic susceptibility $\chi_0(\mathbf{q}_0)$ are derived from calculated or measured band structures and the electron–phonon coupling term $2g^2_{\mathbf{q}_0}/\hbar\omega_{\mathbf{q}_0}$ is deduced from the measured superconducting transition temperature T_{SC}. This approach follows [49]. Note that 1T-TaS$_2$ and 1T-TiSe$_2$ are not superconducting under 'ambient' conditions, but that superconductivity can be induced by hydrostatic pressure in 1T-TaS$_2$ [12] and by Cu intercalation in 1T-TiSe$_2$ [9]—in both cases via suppression of the CDW/PLD phase. We assume here that the novel superconducting states are somewhat characteristic of the pristine, undistorted compounds.

Table 5. Microscopic parameters for the layered CDW compounds 1T-TaS$_2$, 2H-TaSe$_2$ and 1T-TiSe$_2$, as determined from theory and experiment: the non-interacting electronic susceptibility as determined from band structure, electron–phonon coupling parameters as derived from the superconducting transition temperature T_{SC} and band versus lattice energy terms from simple models.

	1T-TaS$_2$	2H-TaSe$_2$	1T-TiSe$_2$
Electronic susceptibility			
$\chi_0(\mathbf{q}_0)/\chi_0(0) - 1$	58%$^{\mathrm{a}}$	35%$^{\mathrm{b}}$	<3%$^{\mathrm{c}}$
$1/\chi_0(\mathbf{q}_0)$ (eV/state)$^{\mathrm{d}}$	0.7–0.9	~0.6	1.3–2.2
Electron–phonon coupling			
T_{SC} (K)	5$^{\mathrm{e}}$	0.15$^{\mathrm{f}}$	4.15$^{\mathrm{g}}$
$\lambda_{\mathrm{McMillan}}{}^{\mathrm{h}}$	0.85	0.49	0.80
$4g^2_{\mathbf{q}_0}/\hbar\omega_{\mathbf{q}_0}$ (eV/state)$^{\mathrm{i}}$	1.0–1.2$^{\mathrm{j}}$	1.3–1.5$^{\mathrm{k}}$	1.6$^{\mathrm{l}}$
Band versus lattice energy			
$-\Delta E_{\mathrm{band}}$ (meV)$^{\mathrm{i}}$	160$^{\mathrm{m}}$	20–26$^{\mathrm{n}}$	20–27$^{\mathrm{o}}$
$-\Delta E_{\mathrm{band}}/\langle u\rangle^2$ (eV Å^{-2})$^{\mathrm{p}}$	3.4$^{\mathrm{q}}$	11.3–15.3	3.7–5.0
$\frac{1}{2}M\omega^2_{\mathbf{q}_0}$ (eV Å^{-2})$^{\mathrm{r}}$	10.0	6.5	2.7

[a] Reference [45]. [b] Reference [114]. [c] Reference [47].

[d] Per transition-metal atom; using $\chi_0(0) = \frac{1}{2}N(0)$ with $N(0)$ values from table 4.

[e] For $p > 3$ GPa [12]. [f] Reference [18]. [g] For Cu$_{0.08}$TiSe$_2$ [9].

[h] Using McMillan's formula, equation (29) [141], with $\mu^* = 0.2$.

[i] Per transition-metal atom.

[j] Using $N(0)$ from LDA, table 4.

[k] Using $N(0)^*$ from specific heat, table 4.

[l] Using $N(0)^* = 1.8$ states/eV u.c. from specific heat [9].

[m] This work. [n] This work and [126]. [o] This work and [23].

[p] Per transition-metal atom; $\langle u\rangle^2$ is the average squared displacement of the transition-metal atoms in the CDW/PLD state. [q] See also [142].

[r] Using the mass of the transition-metal atom for M and the Debye frequency for $\omega_{\mathbf{q}_0}$.

The possibility to estimate the electron–phonon coupling term $2g^2_{\mathbf{q}}/\hbar\omega_{\mathbf{q}}$ from T_{SC} arises because this term appears in the formula for the electron–phonon coupling parameter λ for both the Peierls instability (equation (16)) and BCS superconductivity [141]. In the case of a CDW/PLD, however, the term is taken at the specific wavevector $\mathbf{q} = \mathbf{q}_0$, while for superconductivity it is an average over all wavevectors. We assume that the difference is not substantial. For all three compounds, the measured superconducting transition temperatures are listed in table 5 together with the electron–phonon coupling parameters $\lambda_{\mathrm{McMillan}}$ obtained from the formula [141]

$$\lambda_{\mathrm{McMillan}} = \frac{1.04 + \mu^* \ln\left(\frac{\Theta_D}{1.45T_0}\right)}{(1 - 0.62\mu^*)\ln\left(\frac{\Theta_D}{1.45T_0}\right) - 1.04}. \qquad (29)$$

To determine $\lambda_{\mathrm{McMillan}}$, we assume a Coulomb pseudopotential $\mu^* = 0.2$ and use the Debye temperatures Θ_D listed in table 4. From $\lambda_{\mathrm{McMillan}}$, in turn, $4g^2_{\mathbf{q}_0}/\hbar\omega_{\mathbf{q}_0}$ is estimated via equation (16) using appropriate values of the density of states at the Fermi level, $N(0)$. These are determined from calculated band structures or specific heat measurements and in each case reflect the nature of the state that becomes superconducting (with either an existing or a suppressed CDW).

The remaining terms in condition (9) are the Coulomb repulsion $U_{\mathbf{q}_0}$ and the exchange energy $V_{\mathbf{q}_0}$. These two parameters are not well known, but estimates of $U_{\mathbf{q}_0} \approx 0.4$ eV and $V_{\mathbf{q}_0} \approx 0.4$ eV are consistent with relation (10) and seem reasonable for all three compounds [49].

When all estimated values are finally plugged into relation (9), it turns out that the criterion for CDW/PLD formation is not easily fulfilled for all three systems. Judging from the differences between the left- and right-hand sides of condition (9), the tendency towards CDW/PLD formation is strongest in 2H-TaSe$_2$, intermediate in 1T-TaS$_2$ and weakest in 1T-TiSe$_2$ (see table 5). On the other hand, the term $4g^2_{\mathbf{q}_0}/\hbar\omega_{\mathbf{q}_0}$, which is large when the electron–phonon coupling is strong and the lattice easily deformable, is the largest for 1T-TiSe$_2$. It seems rather important to achieve a small value of $1/\chi_0(\mathbf{q}_0)$. Since the nesting enhancement of $\chi_0(\mathbf{q})$ at $\mathbf{q}_0$ is generally weak, a high density of states at the Fermi level, $N(0)$, is required. For $N(0)$, the order from high to low is again 2H-TaSe$_2$–1T-TaS$_2$–1T-TiSe$_2$ (see table 4). Note, however, that the experimentally observed transition temperatures and CDW/PLD amplitudes suggest the distinct order (from high to low): 1T-TaS$_2$–1T-TiSe$_2$–2H-TaSe$_2$.

In section 4, we have calculated the band structures and spectral weight distributions for the commensurate CDW/PLD phases of 1T-TaS$_2$, 2H-TaSe$_2$ and 1T-TiSe$_2$, using a simple tight-binding scheme. Since the calculated effects are largely consistent with ARPES results, we dare to assume here that the tight-binding band energy changes, δE_{band}, resulting from the PLDs are somehow realistic. The δE_{band} values obtained for the experimentally observed distortion amplitudes are listed in table 5, together with published values, if available. When the results are normalized to the average squared transition-metal atom displacement in the distortion pattern, it is found that the electron–lattice coupling (band energy lowering in eV Å^{-2}) is particularly large in 2H-TaSe$_2$ and by a factor of 3–4 smaller in 1T-TiSe$_2$ and 1T-TaS$_2$.

The counteracting increase in the elastic energy can be modeled by equation (5). If we insert the mass of the transition-metal atom for M and the Debye frequency for the unrenormalized phonon frequency $\omega_{\mathbf{q}_0}$, we can estimate the force constant $M\omega^2_{\mathbf{q}_0}$. The corresponding values are also given in table 5. Since the Debye frequency will be larger than the frequency of the relevant phonon mode, the estimated force constants should be regarded as upper limits.

Comparing the electronic and lattice energy terms, we find that at $T = 0$ a harmonic CDW/PLD instability should definitely occur for 2H-TaSe$_2$ and 1T-TiSe$_2$, but not for 1T-TaS$_2$, the material with the highest transition temperature and the largest CDW/PLD amplitude. We can also estimate the force constants from equation (18). Using the 'universal' value $\Delta(0)/u_{\max} = 0.55 \pm 0.13$ eV Å^{-1} and the $4g^2_{\mathbf{q}_0}/\hbar\omega_{\mathbf{q}_0}$ terms from table 5, we obtain values for $\frac{1}{2}M\omega^2_{\mathbf{q}_0}$ that are smaller than 2 eV Å^{-2} for all three compounds. In this case, harmonic CDW/PLD instability is also attained for 1T-TaS$_2$. But the trend is still inconsistent with the experimental data.

We emphasize that not much confidence should be given to the numbers presented in this section. All estimates are based on crude models and strong approximations and the error bars of some of the involved microscopic parameters are rather large. The goal was to establish trends and identify generally important factors. Unfortunately, the actual order of CDW/PLD strength, as given by the observed transition temperatures or CDW/PLD amplitudes, is reflected neither by the Chan–Heine condition nor by the comparison of band energy and lattice energy changes. The compound with the lowest T_0, 2H-TaSe$_2$, appears to exhibit the strongest tendency towards CDW/PLD formation. The major lessons, then, are that the occurrence of CDW/PLDs in the layered compounds depends on a delicate balance of several factors, that there is not one generally dominant factor (such as $4g^2_{\mathbf{q}_0}/\hbar\omega_{\mathbf{q}_0}$ or $\chi_0(\mathbf{q}_0)$) and that the simple criteria used here do not account for what is experimentally observed.

5.3. Transition temperatures

One may speculate that the Chan–Heine condition (9) fails to provide a coherent picture for the three selected compounds because it is derived in the weak-coupling limit, while, as we have shown in section 3.2, the materials are actually in the intermediate to strong-coupling regime. Here, we will briefly investigate whether the strong-coupling model developed by McMillan for 2H-TaSe$_2$ [39] is in better agreement with the available experimental results.

We focus on a comparison of the transition temperatures predicted by equations (22) and (23), both temperatures being calculated from parameters listed in tables 4 and 5. To simplify the calculation of the strong-coupling T_0 via equation (23), we assume the shortest possible coherence length, $\pi\xi_0 = \lambda_0$, and that the electron–lattice coupling parameter C is given by $|\delta E_{\mathrm{band}}| = Cu_0^2 \ln|E_F/\Delta|^2$ [39]. In figure 14, the predicted and measured T_0 are plotted against the relative lattice distortion u_0/a. Note, again, that there is a conspicuous linear relationship between the experimentally determined T_0 and u_0.

It has been argued that the conventional weak-coupling theory leads to severe inconsistencies in describing the experimental data for the layered compounds [39]. However, figure 14 shows that this statement is exaggerated. Despite the extremely short coherence lengths, the weak-coupling transition temperature, $2\Delta(0)/3.52$, is only by a factor of ~1.6 larger than the experimental values. The reformulated model, in which the strong-coupling limit is assumed, does not, on the whole, provide better agreement. Both models predict the correct order of magnitude of the transition temperature. The

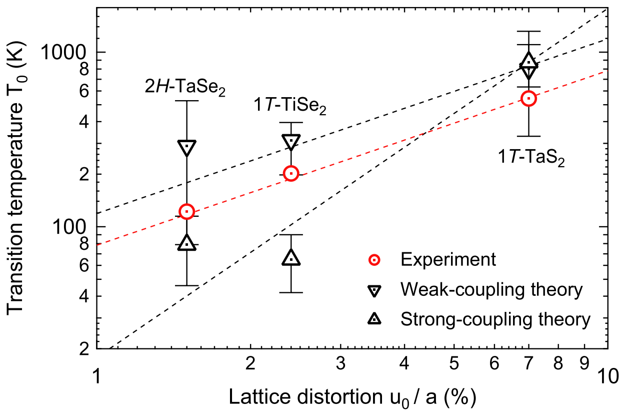

Figure 14. Measured (open circles) and predicted (open triangles) CDW/PLD transition temperatures for 2H-TaSe$_2$, 1T-TiSe$_2$ and 1T-TaS$_2$, plotted against the observed relative lattice distortion (u_0: maximum transition-metal atom displacement, a: lattice constant). The dashed lines are guides to the eye in the spirit of the weak-coupling ($T_0 \propto u_0$) and strong-coupling ($T_0 \propto u_0^2$) theory.

observed quantitative discrepancies may be due to the mean-field approximation [39].

In conclusion, although the wavevectors of the observed CDW/PLD distortions in 1T-TaS$_2$, 2H-TaSe$_2$ and 1T-TiSe$_2$ may somehow fit to the geometry of the electronic structure near E_F and although a local-chemical-bonding picture may provide some clues as to why Ta clusters are formed in 1T-TaS$_2$ and 2H-TaSe$_2$ and why the TiSe$_6$ octahedra distort in a particular way in 1T-TiSe$_2$, these approaches promote qualitative understanding only. Unfortunately, if we want to explain the observed CDW/PLDs in a unified and more quantitative way, we have to rely on simple microscopic theories because realistic total energy calculations are not yet available. For the individual materials, the simple microscopic models and instability criteria are in semi-quantitative agreement with the available experimental data. But the generic trends are not correctly predicted and a coherent explanation in terms of a few **k**-independent parameters has not emerged. Apparently, the CDW/PLDs in the layered compounds are governed by a delicate balance of several factors and, in view of the strongly anisotropic electronic structures, the **k** dependence of these factors cannot be neglected. Further theoretical scrutiny is clearly needed for a quantitative understanding of CDW/PLD formation in the layered transition-metal dichalcogenides.

6. Summary and conclusions

Our goal has been to understand the formation of CDW/PLDs in the layered transition-metal dichalcogenides quantitatively and comprehensively. We first recapitulated the 1D weak-coupling mean-field theory on which much of our understanding is based and, with particular relevance for the layer compounds, restated that our understanding is poor for 2D, anisotropic systems in the strong-coupling regime. In our analysis of real CDW/PLD materials, we then focused on the three prominent layer compounds: 1T-TaS$_2$, 2H-TaSe$_2$ and 1T-TiSe$_2$. We briefly reviewed the large body of experimental and theoretical work on these materials, concentrating on the key signatures of a CDW/PLD: the lattice distortion, the energy gap and the Kohn anomaly. An important conclusion was that the CDW/PLDs observed in the layer compounds are genuinely intermediate coupling to strong coupling in nature. To resolve uncertainties regarding the magnitude and location of the CDW energy gap, we turned to ARPES, which has recently provided an accurate and virtually complete picture of the band structures near the Fermi level, both in the normal phases and in the CDW/PLD phases. We demonstrated that a simple empirical tight-binding model captures the essential aspects of the ARPES spectral weight redistribution and of the underlying band structure changes and we corroborated that, contrary to the simple Peierls model, the electron band energy lowering that stabilizes the CDW/PLD does not result from the opening of a uniform gap at the Fermi vector, but from subband splittings and shifts over extended parts of the Brillouin zone. Finally, we set out to explain CDW/PLD formation in the three selected layer compounds in a unified way on the basis of the simple (knowingly deficient) weak-coupling and strong-coupling mean-field models. Not unexpectedly, the agreement with the experimental data was, at best, semi-quantitative. It turned out that simple considerations based on the geometries of Fermi surfaces or local chemical bonds may serve as qualitative explanations only. Moreover, a generally dominant factor driving CDW/PLD formation could not be identified, although strong electron–phonon coupling and an appropriate density of states near the Fermi level are certainly important. The major conclusion, then, is that the simple, commonly applied theoretical framework, which specifically assumes **k**-independent interactions, fails to describe the situation adequately.

At this point, a significant advance in our understanding of CDW/PLD formation in quasi-2D seems to require greater theoretical and experimental scrutiny. Theory should deliver accurate band structure calculations, providing 3D Fermi surfaces and the **k**-dependent electron–phonon coupling. Also, an accurate treatment of electron–electron and electron–hole interactions is needed. On the other hand, experiment, ARPES in particular, is expected to provide the reality check: accurate and complete band structure data from which accurate experimental maps of the electronic susceptibility can be obtained [85]. It is also foreseen that femtosecond time-resolved ARPES will help to disentangle the relative roles of the various involved interactions in the time domain [14]. In our view, there is reason to believe that it is only difficult and not impossible to understand CDW/PLD formation in the layered transition-metal dichalcogenides quantitatively and comprehensively.

Acknowledgments

The author gratefully acknowledges the contributions by N V Smith (deceased) and thanks M Kalläne for assistance and reading of the manuscript. This work was supported by the Alexander von Humboldt-Stiftung, the Deutsche Forschungsgemeinschaft and the Bundesministerium für Bildung und Forschung. Operation of the Advanced Light

Source is supported by the US Department of Energy, Office of Basic Energy Sciences.

References

[1] Peierls R E 1955 *Quantum Theory of Solids* (Oxford: Clarendon) pp 108–12
Peierls R E 1991 *More Surprises in Theoretical Physics* (Princeton, NJ: Princeton University Press) pp 27–30
[2] Fröhlich H 1954 *Proc. R. Soc.* A **233** 296
[3] Overhauser A W 1968 *Phys. Rev.* **167** 691
Overhauser A W 1971 *Phys. Rev.* B **3** 3173
Overhauser A W 1978 *Adv. Phys.* **27** 353
[4] Kohn W 1968 *Many Body Physics* ed C DeWitt and R Balian (New York: Gordon and Breach) p 353
[5] Halperin B I and Rice T M 1968 *Solid State Phys.* **21** 115
Halperin B I and Rice T M 1968 *Rev. Mod. Phys.* **40** 755
[6] Chan S-K and Heine V 1973 *J. Phys. F: Met. Phys.* **3** 795
[7] Tosatti E 1975 *Festkörperprobleme* (*Advances in Solid State Physics* vol 15) ed H J Queisser (Braunschweig: Vieweg) p 113
[8] Friedel J 1977 *Electron–Phonon Interactions and Phase Transitions* ed T Riste (New York: Plenum) p 1
[9] Morosan E, Zandbergen H W, Dennis B S, Bos J W G, Onose Y, Klimczuk T, Ramirez A P, Ong N P and Cava R J 2006 *Nature Phys.* **2** 544
[10] Kiss T, Yokoya T, Chainani A, Shin S, Hanaguri T, Nohara M and Takagi H 2007 *Nature Phys.* **3** 720
[11] Cercellier H *et al* 2007 *Phys. Rev. Lett.* **99** 146403
[12] Sipos B, Kusmartseva A F, Akrap A, Berger H, Forró L and Tutiš E 2008 *Nat. Mater.* **7** 960
[13] Johannes M D and Mazin I I 2008 *Phys. Rev.* B **77** 165135
[14] Schmitt F *et al* 2008 *Science* **321** 1649
[15] Yusupov R, Mertelj T, Kabanov V V, Brazovskii S, Kusar P, Chu J-H, Fisher I R and Mihailovic D 2010 *Nature Phys.* **6** 681
[16] Hellmann S *et al* 2010 *Phys. Rev. Lett.* **105** 187401
[17] Eichberger M, Schäfer H, Krumova M, Beyer M, Demsar J, Berger H, Moriena G, Sciaini G and Miller R J D 2010 *Nature* **468** 799
[18] Wilson J A, Di Salvo F J and Mahajan S 1975 *Adv. Phys.* **24** 117
[19] Friend R H and Jérome D 1979 *J. Phys. C: Solid State Phys.* **12** 1441
[20] Di Salvo F J and Rice T M 1979 *Phys. Today* **32** 32
[21] Klipstein P C, Friend R H and Yoffe A D 1985 *Phil. Mag.* B **52** 611
[22] Withers R L and Wilson J A 1986 *J. Phys. C: Solid State Phys.* **19** 4809
[23] Motizuki K (ed) 1986 *Structural Phase Transitions in Layered Transition Metal Compounds* (Dordrecht: Reidel)
[24] Whangbo M-H and Canadell E 1992 *J. Am. Chem. Soc.* **114** 9587
[25] Grüner G 2000 *Density Waves in Solids* (Cambridge, MA: Perseus)
[26] Brouet V, Yang W L, Zhou X J, Hussain Z, Ru N, Shin K Y, Fisher I R and Shen Z X 2004 *Phys. Rev. Lett.* **93** 126405
[27] Brouet V *et al* 2008 *Phys. Rev.* B **77** 235104
[28] Grüner G 1988 *Rev. Mod. Phys.* **60** 1129
[29] Gabovich A M, Voitenko A I and Ausloos M 2002 *Phys. Rep.* **367** 583
[30] Aruga T 2002 *J. Phys.: Condens. Matter* **14** 8393
[31] Littlewood P B 1983 *Crit. Rev. Solid State Mater. Sci.* **11** 229
[32] Fawcett E 1988 *Rev. Mod. Phys.* **60** 209
[33] Altmann S L 1994 *Band Theory of Solids: An Introduction from the Point of View of Symmetry* (Oxford: Clarendon) chapter 12
[34] Rice M J and Strässler S 1973 *Solid State Commun.* **13** 125
[35] Allender D, Bray J W and Bardeen J 1974 *Phys. Rev.* B **9** 119
[36] Littlewood P B and Heine V 1981 *J. Phys. C: Solid State Phys.* **14** 2943
[37] Tosatti E 1995 *Electronic Surface and Interface States on Metallic Systems* ed E Berthel and M Donath (Singapore: World Scientific) p 67
[38] Tosatti E 1980 *Modern Trends in the Theory of Condensed Matter* ed A Pekalski and J Przystawa (Berlin: Springer) p 501
[39] McMillan W L 1977 *Phys. Rev.* B **16** 643
Riste T (ed) 1977 *Electron–Phonon Interactions and Phase Transitions* (New York: Plenum) p 142
[40] Haas C 1978 *Solid State Commun.* **26** 709
[41] Inglesfield J E 1980 *Physica* B **99** 238
[42] Huntley D J, DiSalvo F J and Rice T M 1978 *J. Phys. C: Solid State Phys.* **11** L767
[43] Fehlner W R and Loly P D 1974 *Solid State Commun.* **14** 653
[44] Rice T M and Scott G K 1975 *Phys. Rev. Lett.* **35** 120
[45] Myron H W, Rath J and Freeman A J 1977 *Phys. Rev.* B **15** 885
[46] Doran N J, Riccó B, Schreiber M, Titterington D and Wexler G 1978 *J. Phys. C: Solid State Phys.* **11** 699
[47] Yoshida Y and Motizuki K 1980 *J. Phys. Soc. Japan* **49** 898
[48] Motizuki K and Ando E 1983 *J. Phys. Soc. Japan* **52** 2849
[49] Doran N J, Wexler G, Heine V and Ricco B 1977 *Nuovo Cimento* B **38** 544
[50] Varma C M and Weber W 1977 *Phys. Rev. Lett.* **39** 1049
[51] Yoshida Y and Motizuki K 1982 *J. Phys. Soc. Japan* **51** 2107
[52] Doran N J 1978 *J. Phys. C: Solid State Phys.* **11** L959
[53] Rice M J and Gartstein Y N 2005 *J. Phys.: Condens. Matter* **17** 4615
[54] Neuenschwander J and Wachter P 1990 *Phys. Rev.* B **41** 12693
[55] Gaby J H, DeLong B, Brown F C, Kirby R D and Lévy F 1981 *Solid State Commun.* **39** 1167
[56] Wilson J A, Di Salvo F J and Mahajan S 1974 *Phys. Rev. Lett.* **32** 882
[57] Dai Z, Xue Q, Gong Y, Slough C G and Coleman R V 1993 *Phys. Rev.* B **48** 14543
[58] Tatlock G J 1976 *Commun. Phys.* **1** 87
[59] Bayliss S C, Ghorayeb A M and Guy D R P 1984 *J. Phys. C: Solid State Phys.* **17** L533
[60] DiSalvo F J, Moncton D E, Wilson J A and Mahajan S 1976 *Phys. Rev.* B **14** 1543
[61] Scruby C B, Williams P M and Parry G S 1975 *Phil. Mag.* **31** 255
[62] Brouwer R and Jellinek F 1980 *Physica* B **99** 51
[63] Spijkerman A, de Boer J L, Meetsma A, Wiegers G A and van Smaalen S 1997 *Phys. Rev.* B **56** 13757
[64] Fung K K, Steeds J W and Eades J A 1980 *Physica* B +C **99** 47
[65] Tanda S, Sambongi T, Tani T and Tanaka S 1984 *J. Phys. Soc. Japan* **53** 476
[66] Nakanishi K and Shiba H 1984 *J. Phys. Soc. Japan* **53** 1103
[67] Fazekas P and Tosatti E 1979 *Phil. Mag.* B **39** 229
Fazekas P and Tosatti E 1980 *Physica* B **99** 183
[68] Dardel B, Grioni M, Malterre D, Weibel P, Baer Y and Lévy F 1992 *Phys. Rev.* B **45** 1462
Dardel B, Grioni M, Malterre D, Weibel P, Baer Y and Lévy F 1992 *Phys. Rev.* B **46** 7407
[69] Moncton D E, Axe J D and DiSalvo F J 1977 *Phys. Rev.* B **16** 801
[70] Fleming R M, Moncton D E, McWhan D B and DiSalvo F J 1980 *Phys. Rev. Lett.* **45** 576
[71] DiSalvo F J, Moncton D E and Waszczak J V 1976 *Phys. Rev.* B **14** 4321
[72] McMillan W L 1975 *Phys. Rev.* B **12** 1187
McMillan W L 1976 *Phys. Rev.* B **14** 1496
Riste T (ed) 1977 *Electron–Phonon Interactions and Phase Transitions* (New York: Plenum) p 137

[73] Nakanishi K and Shiba H 1977 *J. Phys. Soc. Japan* **43** 1839
Nakanishi K and Shiba H 1978 *J. Phys. Soc. Japan* **44** 1465
Shiba H and Nakanishi K 1986 *Structural Phase Transitions in Layered Transition Metal Compounds* ed K Motizuki (Dordrecht: Reidel) p 175

[74] Withers R L and Bursill L A 1982 *Phys. Rev.* B **26** 1469

[75] Smith N V, Kevan S D and DiSalvo F J 1985 *J. Phys. C: Solid State Phys.* **18** 3175

[76] Enomoto H, Ozaki H, Suzuki M, Fujii T and Yamaguchi M 1991 *J. Vac. Sci. Technol.* B **9** 1022

[77] Pillo Th, Hayoz J, Naumović D, Berger H, Perfetti L, Gavioli L, Taleb-Ibrahimi A, Schlapbach L and Aebi P 2001 *Phys. Rev.* B **64** 245105

[78] Gasparov L V, Brown K G, Wint A C, Tanner D B, Berger H, Margaritondo G, Gaál R and Forró L 2002 *Phys. Rev.* B **66** 094301

[79] Aiura Y *et al* 2004 *Phys. Rev.* B **69** 245123

[80] Wang C, Giambattista B, Slough C G, Coleman R V and Subramanian M A 1990 *Phys. Rev.* B **42** 8890

[81] Liu R, Olson C G, Tonjes W C and Frindt R F 1998 *Phys. Rev. Lett.* **80** 5762

[82] Liu R, Tonjes W C, Greanya V A, Olson C G and Frindt R F 2000 *Phys. Rev.* B **61** 5212

[83] Demsar J, Forró L, Berger H and Mihailovic D 2002 *Phys. Rev.* B **66** 041101(R)

[84] Rossnagel K, Rotenberg E, Koh H, Smith N V and Kipp L 2005 *Phys. Rev.* B **72** 121103(R)

[85] Borisenko S V *et al* 2008 *Phys. Rev. Lett.* **100** 196402

[86] Rossnagel K, Kipp L and Skibowski M 2001 *Phys. Rev.* B **65** 235101

[87] Kidd T E, Miller T, Chou M Y and Chiang T-C 2002 *Phys. Rev. Lett.* **88** 226402

[88] Qian D, Hsieh D, Wray L, Morosan E, Wang N L, Xia Y, Cava R J and Hasan M Z 2007 *Phys. Rev. Lett.* **98** 117007

[89] Zhao J F *et al* 2007 *Phys. Rev. Lett.* **99** 146401

[90] Machida Y, Hanashima T, Ohkubo K, Yamawaki K, Tanaka M and Sasaki S 2004 *J. Phys. Soc. Japan* **73** 3064

[91] Holt M, Zschack P, Hong H, Chou M Y and Chiang T-C 2001 *Phys. Rev. Lett.* **86** 3799

[92] Bovet M, van Smaalen S, Berger H, Gaal R, Forró L, Schlapbach L and Aebi P 2003 *Phys. Rev.* B **67** 125105

[93] Krasovskii E E 2007 private communication

[94] Reshak A H and Auluck S 2005 *Physica* B **358** 158

[95] Reshak A H and Auluck S 2003 *Phys. Rev.* B **68** 245113

[96] Shiino O *et al* 2000 *Physica* B **284–288** 1673

[97] Harper J M E, Geballe T H and DiSalvo F J 1977 *Phys. Rev.* B **15** 2943

[98] Craven R A, Di Salvo F J and Hsu F S L 1978 *Solid State Commun.* **25** 39

[99] Ruzicka B, Degiorgi L, Berger H, Gaál R and Forró L 2001 *Phys. Rev. Lett.* **86** 4136

[100] Hambourger P D and Di Salvo F J 1980 *Physica* B **99** 173

[101] Lieth R M A and Terhell J C J M 1977 *Preparation and Crystal Growth of Materials with Layered Structures* ed R M A Lieth (Dordrecht: Reidel) p 141

[102] Ashcroft N W and Mermin N D 1976 *Solid State Physics* (Fort Worth: Saunders)

[103] Naito M and Tanaka S 1982 *J. Phys. Soc. Japan* **51** 219

[104] Zwick F, Berger H, Vobornik I, Margaritondo G, Forró L, Beeli C, Onellion M, Panaccione G, Taleb-Ibrahimi A and Grioni M 1998 *Phys. Rev. Lett.* **81** 1058

[105] Pillo T, Hayoz J, Berger H, Grioni M, Schlapbach L and Aebi P 1999 *Phys. Rev. Lett.* **83** 3494

[106] Pillo Th, Hayoz J, Berger H, Fasel R, Schlapbach L and Aebi P 2000 *Phys. Rev.* B **62** 4277

[107] Aebi P, Pillo T, Berger H and Lévy F 2001 *J. Electron Spectrosc. Relat. Phenom.* **117/118** 433

[108] Bovet M, Popović D, Clerc F, Koitzsch C, Probst U, Bucher E, Berger H, Naumović D and Aebi P 2004 *Phys. Rev.* B **69** 125117

[109] Arita M *et al* 2004 *Physica* B **351** 265

[110] Perfetti L, Gloor T A, Mila F, Berger H and Grioni M 2005 *Phys. Rev.* B **71** 153101

[111] Clerc F, Battaglia C, Bovet M, Despont L, Monney C, Cercellier H, Garnier M G and Aebi P 2006 *Phys. Rev.* B **74** 155114

[112] Clerc F, Battaglia C, Cercellier H, Monney C, Berger H, Despont L, Garnier M G and Aebi P 2007 *J. Phys.: Condens. Matter* **19** 355002

[113] Inosov D S, Zabolotnyy V B, Evtushinsky D V, Kordyuk A A, Büchner B, Follath R, Berger H and Borisenko S V 2008 *New J. Phys.* **10** 125027

[114] Inosov D S, Evtushinsky D V, Zabolotnyy V B, Kordyuk A A, Büchner B, Follath R, Berger H and Borisenko S V 2009 *Phys. Rev.* B **79** 125112

[115] Pillo Th, Hayoz J, Berger H, Lévy F, Schlapbach L and Aebi P 2000 *Phys. Rev.* B **61** 16213

[116] Rasch J C E, Stemmler T, Müller B, Dudy L and Manzke R 2008 *Phys. Rev. Lett.* **101** 237602

[117] Mattheiss L F 1973 *Phys. Rev.* B **8** 3719

[118] Rossnagel K and Smith N V 2006 *Phys. Rev.* B **73** 073106

[119] Rossnagel K and Smith N V 2007 *Phys. Rev.* B **76** 073102

[120] Barnett R L, Polkovnikov A, Demler E, Yin W-G and Ku W 2006 *Phys. Rev. Lett.* **96** 026406

[121] Abate E and Asdente M 1965 *Phys. Rev.* **140** A1303

[122] Herman F and Skillman S 1963 *Atomic Structure Calculations* (Englewood Cliffs, NJ: Prentice-Hall)

[123] Harrison W A 2004 *Elementary Electronic Structure* revised edn (Singapore: World Scientific)

[124] Voit J, Perfetti L, Zwick F, Berger H, Margaritondo G, Grüner G, Höchst H and Grioni M 2000 *Science* **290** 501

[125] Grioni M, Ast C R, Pacilé D, Papagno M, Berger H and Perfetti L 2005 *New J. Phys.* **7** 106

[126] Doran N J and Woolley A M 1981 *J. Phys. C: Solid State Phys.* **14** 4257

[127] Anderson O, Manzke R and Skibowski M 1985 *Phys. Rev. Lett.* **55** 2188

[128] van Wezel J, Nahai-Williamson P and Saxena S S 2010 *Phys. Rev.* B **81** 165109

[129] van Wezel J, Nahai-Williamson P and Saxena S S 2010 *Europhys. Lett.* **89** 47004

[130] van Wezel J, Nahai-Williamson P and Saxena S S 2010 *Phys. Status Solidi* b **247** 592

[131] Thompson A H 1976 *Comm. Solid State Phys.* **7** 125

[132] Di Salvo F J 1977 *Electron–Phonon Interactions and Phase Transitions* ed T Riste (New York: Plenum) p 107

[133] Wertheim G K, Di Salvo F J and Chiang S 1976 *Phys. Rev.* B **13** 5476

[134] Coleman R V, Giambattista B, Hansma P K, Johnson A, McNairy W W and Slough C G 1988 *Adv. Phys.* **37** 559

[135] Hughes H P 1977 *J. Phys. C: Solid State Phys.* **10** L319

[136] Suzuki N, Yamamoto A and Motizuki K 1984 *Solid State Commun.* **49** 1039

[137] Wilson J A and Mahajan S 1977 *Commun. Phys.* **2** 23

[138] Wilson J A 1977 *Solid State Commun.* **22** 551
Wilson J A 1978 *Phys. Status Solidi* b **86** 11

[139] Monney C *et al* 2009 *Phys. Rev.* B **79** 045116

[140] Monney C *et al* 2010 *Phys. Rev.* B **81** 155104

[141] McMillan W C 1968 *Phys. Rev.* **167** 331

[142] Inglesfield J E 1980 *J. Phys. C: Solid State Phys.* **13** 17